Microfluidic synthesis and assembly of noble metal nanoparticles for surface-enhanced vibrational spectroscopies

Gustavo Ochoa

To cite this version:

Gustavo Ochoa. Microfluidic synthesis and assembly of noble metal nanoparticles for surface-enhanced vibrational spectroscopies. Material chemistry. Université de Bordeaux; Universidad autónoma de Nuevo León, 2022. English. NNT : 2022BORD0096 . tel-03739895

HAL Id: tel-03739895
https://theses.hal.science/tel-03739895v1

Submitted on 28 Jul 2022

université de BORDEAUX

UANL
UNIVERSIDAD AUTÓNOMA DE NUEVO LEÓN

COTUTELLE THESIS PRESENTED
TO OBTAIN THE GRADE OF

DOCTOR OF THE UNIVERSITY OF BORDEAUX AND THE AUTONOMOUS UNIVERSITY OF NUEVO LEON

DOCTORAL SCHOOL OF SCIENCE OF CHEMISTRY, FIELD: PHYSICO-CHEMISTRY OF CONDENSED MATTER
FACULTY OF SCIENCE OF CHEMISTRY, FIELD: MATERIAL CHEMISTRY

BY

GUSTAVO OCHOA VAZQUEZ

MICROFLUIDIC SYNTHESIS AND ASSEMBLY OF NOBLE METAL NANOPARTICLE FOR SURFACE-ENHANCED VIBRATIONAL SPECTROSCOPIES

Under the direction of Dr. Israel López, Dr. Boris Kharissov and Dr. Samuel Marre

Thesis dissertated in March 2022
under review by the following jury:

Mme. Nora Aleyda GARCÍA-GÓMEZ	Research Professor – Centro de Investigación en Biotecnología y Nanotecnología	Examinateur
Mme. Ana María ARIZMENDI-MORQUECHO	Research Professor - Centro de Investigación de Materiales Avanzados	Rapporteur
M. Ali ABOU-HASSAN	Associate Professor – Sorbonne University	Examinateur
M. Samuel MARRE	Research Director – Bordeaux University	Thesis Director
M. Israel Alejandro LÓPEZ-HERNÁNDEZ	Research Professor – Centro de Investigación en Biotecnología y Nanotecnología	Thesis Director
M. Omar Eduardo LÓPEZ-BOTELLO	Research Professor – Instituto Tecnológico de Monterrey	Rapporteur

SYNTHESE MICROFLUIDIQUE ET ASSEMBLAGE DE NANOPARTICULES DE METAUX NOBLES POUR LES SPECTROSCOPIES VIBRATIONNELLES AMELIOREES EN SURFACE

Résumé : Dans le présent travail, différents réacteurs microfluidiques ont été conçus et fabriqués pour la synthèse microfluidique de nanoparticules d'Ag et d'Au, en utilisant un système de génération de gouttelettes par flux segmenté. Tout d'abord, la fabrication de dispositifs microfluidiques PDMS/verre a été réalisée en utilisant la méthode de lithographie douce qui permet leur obtention de manière reproductible. Cependant, le mélange des propriétés de surface entre les matériaux ne permettait pas de contrôler la reproductibilité des synthèses en raison de problèmes de colmatage à travers les canaux et de coalescence au sein des gouttelettes, provoquant des perturbations de vitesses sur les fluides, et des dépôts de croissance d'Ag au sein des canaux.

Pour cette raison, un réacteur microfluidique tubulaire a été fabriqué. Ceci, ayant la même propriété de surface dans tout le réacteur, a permis l'obtention de nanoparticules d'Ag et d'Au avec des morphologies sphériques et des tailles de 7 et 15 nm, respectivement. De plus, ces nanoparticules présentaient un LSPR à 400 nm pour Ag et 520 nm pour Au, caractéristiques de ces métaux.

D'autre part, les dispositifs microfluidiques Si/Pyrex sont conditionnés et fabriqués pour une utilisation ultérieure en tant que substrat microfluidique SERS. Celles-ci ont été fonctionnalisées par un procédé de silanisation avec du 3-mercaptopropyltriméthoxysilane pour assembler les nanoparticules de métaux nobles à la surface de leurs microcanaux.

Par la suite, des nanoparticules d'Au ont été passées à travers les microcanaux des dispositifs microfluidiques à 80 µL h-1, puis du 4-aminothiophénol a été passé à 20 µL h-1 comme molécule test pour son évaluation dans la spectroscopie Raman augmentée sur des surfaces, en observant une analyse facteur de grossissement de 17 sur les signaux caractéristiques de cette molécule à 1590 et 1080 cm-1, concluant que la synthèse et l'assemblage microfluidique de nanoparticules de métaux nobles est une alternative pour l'analyse SERS.

Mots clés : Microfluidique, Synthèse microfluidique, Nanoparticules de métaux nobles, Nanoparticules d'argent, Nanoparticules d'or, SERS.

MICROFLUIDIC SYNTHESIS AND ASSEMBLY OF NOBLE METAL NANOPARTICLE FOR SURFACE-ENHANCED VIBRATIONAL SPECTROSCOPIES

Abstract : In the present work, different microfluidic reactors were designed and fabricated for the microfluidic synthesis of Ag and Au nanoparticles, using a droplet generation system through segmented flow. First, the fabrication of PDMS/glass microfluidic devices was carried out using the soft lithography method which allow their obtainment in a reproducible way. However, the mixture of surface properties between the materials did not allow to control the reproducibility of the syntheses due to clogging problems through the channels and coalescence within the droplets, causing velocities disruptions on the fluids, and Ag growth deposits within the channels.

Because of this, a tubular microfluidic reactor was fabricated. This, having the same surface property throughout the reactor, allowed the obtaining of Ag and Au nanoparticles with spherical morphologies and sizes of 7 and 15 nm, respectively. In addition, these nanoparticles presented an LSPR at 400 nm for Ag and 520 nm for Au, characteristics of these metals.

On the other hand, Si/Pyrex microfluidic devices are conditioned and manufactured for later use as a SERS microfluidic substrate. These were functionalized through a silanization process with 3-mercaptopropyltrimethoxysilane to assemble the noble metal nanoparticles on the surface of their microchannels.

Subsequently, Au nanoparticles were flowed through the microchannels of the microfluidic devices at 80 µL h^{-1} and then 4-aminothiophenol was flowed at 20 µL h^{-1} as a test molecule for its evaluation in the augmented Raman spectroscopy on surfaces, observing An analytical magnification factor of 17 on the characteristic signals of this molecule at 1590 and 1080 cm^{-1}, concluding that the synthesis and microfluidic assembly of noble metal nanoparticles is an alternative for SERS analysis.

Keywords : Microfluidics, Microfluidic Synthesis, Noble Metal Nanoparticles, Silver Nanoparticles, Gold Nanoparticles, SERS.

SÍNTESIS Y ENSAMBLE MICROFLUÍDICO DE NANOPARTÍCULAS DE METALES NOBLES PARA ESPECTROSCOPIA VIBRACIONAL AUMENTADAS EN SUPERFICIE

Resumen : En el presente trabajo se diseñaron y fabricaron distintos reactores microfluídicos para la síntesis microfluídica de nanopartículas de Ag y Au empleando un sistema de generación de gotas mediante flujo segmentado. Primeramente, la fabricación de dispositivos microfluídicos de PDMS/vidrio se llevó a cabo empleando el método de softlithography, el cual permitió la obtención de éstos de manera reproducible. Sin embargo, la mezcla de propiedades superficiales entre los materiales no permitió controlar la reproducibilidad de las síntesis debido a problemas de obstrucción en los canales y coalescencia dentro de las gotas, provocando variaciones en las velocidades de los fluidos y crecimiento de depósitos de Ag dentro de los canales.

Debido a esto, se fabricó un reactor microfluídico tubular. Éste, al tener la misma propiedad superficial en todo el reactor, permitió la obtención de nanopartículas de Ag y Au con morfologías esféricas y de tamaños de 7 y 15 nm, respectivamente. Además, estas nanopartículas presentaron una LSPR a 400 nm para Ag y 520 nm para el Au, características de estos metales.

Por otro lado, se diseñó y fabrico dispositivos microfluídicos de Si/Pyrex para su posterior uso como sustrato microfluídico SERS. Estos se funcionalizaron mediante un proceso de silanización con 3-mercaptopropiltrimetoxisilano con el fin de ensamblar las nanopartículas de metales nobles sobre la superficie de sus microcanales.

Posteriormente, se fluyeron nanopartículas de Au a través de los microcanales de los dispositivos mcirofluidicos a 80 µL h^{-1} y después se fluyó 4-aminotiofenol a 20 µL h^{-1} como molécula prueba para su evaluación en la espectroscopía Raman aumentada en superficies, observando un factor de aumento analítico de 17 sobre las señales características de esta molécula a 1590 y 1080 cm-1, concluyendo que la síntesis y ensemble microfluídico de nanopartículas de metales nobles es una alternativa para el análisis en SERS.

Palabras clave : Microfluídica, Síntesis Microfluídica, Nanopartículas de Metales Nobles, Nanopartículas de Plata, Nanopartículas de Oro, SERS.

WORKPLACE

The present research work was developed in the Nanoscience and Nanotechnology Laboratory of the Centro de Investigación en Biotecnología y Nanotecnología, CIBYN, as well as in the Big Mac Lab of the Institut de Chimie de la Matière Condensée de Bordeaux, ICMCB as a part of double degree program between the Universidad Autónoma de Nuevo León and the Université de Bordeaux under the supervision of Dr. Israel Alejandro López-Hernández and Dr. Samuel Marre.

During the stay in Mexico, the disposal and handling of waste was carried out according to the safety and hygiene standards of the Faculty of Chemical Sciences of the Autonomous University of Nuevo León. Similarly, the ICMCB's safety and hygiene regulations were respected during the stay in France.

DEDICATION

To my parents,

Gustavo Ochoa Leal and Guadalupe Vazquez Esquivel

For their unconditional love.

To my beloved Juany Nava,

for her love and understanding.

You are my wonder.

ACKNOWLEDGMENT

To the Universidad Autónoma de Nuevo León and Université de Bordeaux due to all the facilities in my doble degree program between them.

To the CONACYT and La CAF for the scholarship and the financial assistance during all my PhD and stay in France.

To Dr. Nora García, Dr. Luis C. Torres and Dr. Ana Arizmendi, for bring me guidance during my research work as well as ***Dr. Ali Abou Hassan and Dr. Laurent Servant*** for their advises.

To Dr. Israel López and Dr. Samuel Mare for believe and encourage me to get the best of myself. For your patient, good advice and confidence.

To all my friends who, in some way, supported me when I needed it most**:** Arturo Heredia, Francisco Acosta, Osmani Rodríguez, Alejandro Pacheco, Williams González, Alfonso Balderas, Antonio Esparza, Susana Borbón, Carlos Puente, Luis Serna, Francisco Borja, Laurin Kennel, Thomas Jahouari, Elen Duverger-MacDellec ***but specially to Juany Nava*** for never leave me alone and letting go my hand, even at a distance.

INDEX

TABLE LIST

FIGURE LIST

NOMENCLATURE

3-MPTMS	3-Mercaptopropyl trimethoxy silane
4-ATP	4-Aninothiophenol
BH^{4-}	Borohydride ion
Ca	Capillary number
°C	Celsius degrees
$HAuCl_4$	Chloroauric acid
Cit^{3-}	Citrate ion
Ø	Diameter
Au	Gold
Au^{3+}	Gold ion

g	Grams
h	Hours
I.D.	Inner diameter
Kg	Kilograms
L	Liter
LSPR	Located Surfaces Plasmon Resonance
µm	Microliter
µm	Micrometer
mL	Milliliter
mm	Millimeter
mg	Milligrams
mL/h	Milliliter per hour
mM	Millimolar

min	Minutes
M	Molar
NPs	Nanoparticles
nm	Nanometer
O.D.	Outside diameter
PDMS	Polydimethylsiloxane
PEEK	Polyether ether ketone
RT	Residence time
rpm	Revolutions per minute
Re	Reynolds number
s	Seconds
Si	Silicone
SiO_2	Silicone oxide

Ag	Silver
Ag^+	Silver ion
$AgNO_3$	Silver nitrate
$NaBH_4$	Sodium borohydride
Na^3Cit	sodium citrate
SEIRAS	Surface-Enhanced Infrared Absorption Spectroscopy
SERS	Surface-Enhanced Raman Spectroscopy
SEVS	Surface-Enhanced Vibrational Spectroscopies
TEM	Transmission electron microscopy
λ	wavelength
%wt.	weight percentage

CHAPTER I

INTRODUCTION

Nowadays, the world is in constant change and some decision in politics, society and economics have treated to increase the social insecurity, the public health problems, and the environmental pollution. For example, in Mexico, marijuana, cocaine and heroin are trafficked to the USA and represent 90% of consumed drugs in this country[1]. Only in 2016, 8000 ton was produced and export to USA, Canada, and Europe. Also, the present drug-gun trade between Mexico and the USA is growing up according to “fast and furious” operation, demonstrating that is important to detect compounds related to this trafficking[2].

On the other hand, in a globally way, fast and trace level analysis are necessary for try to reduce death rates and to detect diseases in a timely manner and thus provide care as soon as possible. Nowadays, cancer and tuberculosis are two of ten death cause. Only in 2018, 9.6 million people died because of cancer[3] and, in 2017, 10 million of people died because of tuberculosis[4].

Environmental incidents are another global problem. For example, the contamination by pesticides in soils, water, and air as such as in agriculture products as fruits and vegetables are causer of 200,000 death per year, according to WHO study[5]. For to resolve this kind of problem, are necessary to develop methodologies that allow to detect this kind of molecules in trace levels in real samples.

For all these reasons, is important an opportune detection of drug and/or firearms components, viruses and cancer antigens and polluting agents in air, water, and soil as pesticides in a trace level. Exist chemical methods and instrumental techniques for elucidating chemical spices and quantify them in trace levels, highlighting these latter for their limit of detection and reliability. In instrumental techniques, we can emphasize the vibrational spectroscopies for their easy operation and molecule information that they give.

1.1. Vibrational Spectroscopies

Molecule characterizations and chemical reactions can be studied using spectroscopies techniques. For this, vibrational spectroscopies (VS) make use of matter-light interactions, using particular energies of electromagnetic radiation and observing absorbed, transmitted or scattered from the sample[6]. For this, we need considerate the experimental work by Einstein, Planck and Bohr, where they demonstrated that electromagnetic radiation could be regarded as a stream of particles, called *quanta*, where its energy is given by the Bohr equation:

$$E = hv \tag{1}$$

Where h is the Planck's constant, and v is the frequency of that radiation. Also, this vibration process can be represented in terms of quantized discrete energy levels as well as in frequency terms.

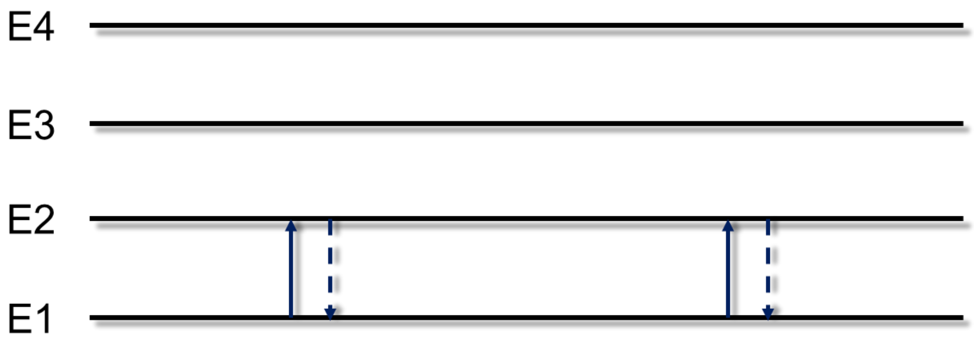

Figure 1. Discrete and quantized energy levels.

Whenever exist a matter-light interaction, a quantum of energy is emitted or absorbed when this energy of incident radiation match and fit exactly the energy gap between two energy levels (Figure 1). This is related to the frequency by:

$$\Delta E = hv \tag{2}$$

And for the $E_0 - E_1$ gap:

$$v = (E_1 - E_0)/h \tag{3}$$

However, is common to promote an electron from its ground state (GS) to excited states (ES) using electromagnetic radiation, but in VS the incident radiations employed have low energies, producing vibrational states, as we can see in Figure 2. In this process, the energy absorbed is not the necessary for fill the gap between the GS and ES[7].

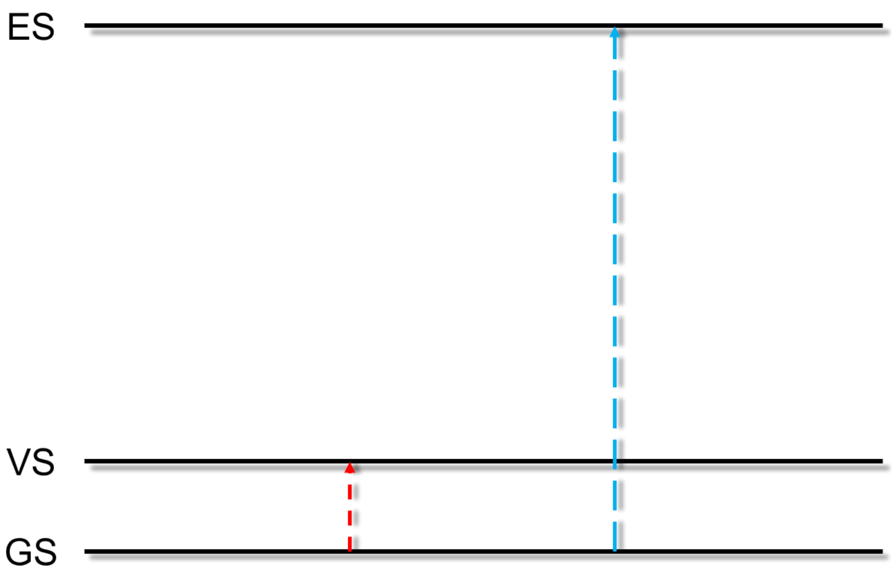

Figure 2. Energy Diagram.

In a vibrational state, the molecules bonding is stretched, flexion and/or contracted as a response to energy absorption from the incident radiation. On the other hand, with some specific electromagnetic radiation, we can vibrate the molecule electron cloud in different directions and some VS techniques, as Infrared Spectroscopy and Raman Spectroscopy, use this vibrational information for elucidate molecule structure and, some cases, quantify it[8].

1.1.1. Infrared Spectroscopy

A widely used technique for molecule characterization as well as functional groups characterization is the Infrared Spectroscopy. This VS uses a specific electromagnetic field region called Infrared region (IR) for analysis. This IR, in terms of wavelength, is between 7.8×10^{-5} to 3×10^{-2} cm, however, these limits are in constant discussion for the scientific community[9].

In Infrared spectroscopy, a phenomenon of absorption occurs when the sample interacts with the IR radiation. In terms of frequency, when IR radiation match with the energy of a specific molecular vibration, absorbs occurs. However, for this phenomenon, the molecule probe must have a change in its electric dipole moment during the vibrational process.

For a molecule can be infrared-active, is necessary it has a permanent dipole moment. For heteronuclear diatomic molecules, this vibrational process occurs changing the electric dipole moment, expanding, or contracting the molecule bond, generating a characteristic vibrational mode. On the other hand, homonuclear diatomic molecules do not present vibrational modes at IR frequencies due to its electric dipole moment remains zero[10].

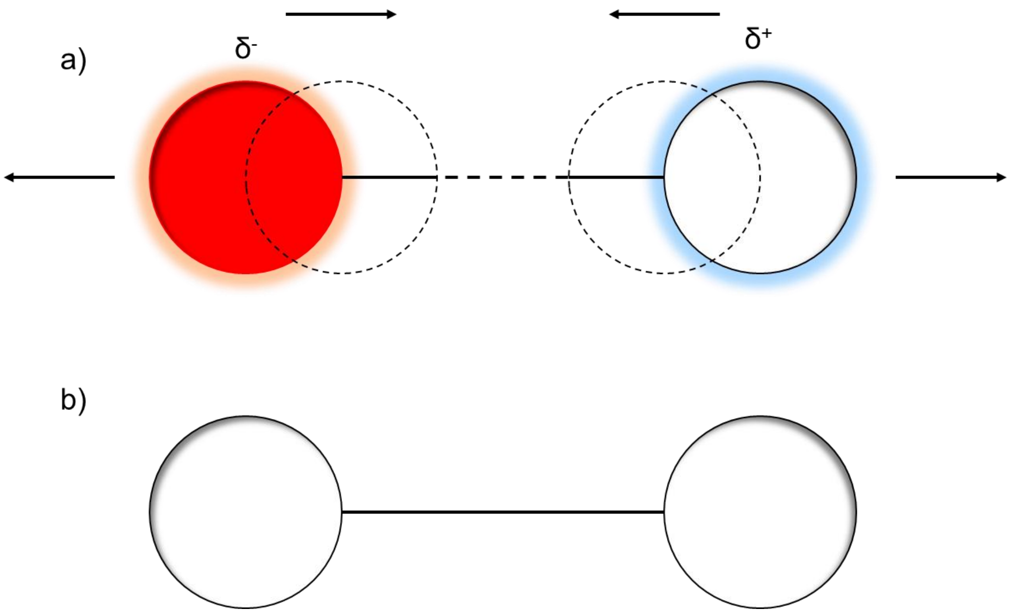

Figure 3. a) Infrared-active molecule. b) Non-infrared-active molecule.

Hence, to understand these molecular vibrations, we can see the molecule probe as a system of masses joined by springs. Their vibrations are closely related to the stiffness of the bond and the masses of the atoms[7]. This stiffness of the bond can be characterized by a constant term, derived from Hook’s law, called force constant, K. Classically, the equation 4 can explain the vibrational frequency for a diatomic molecule:

$$v = \frac{1}{2\pi}\sqrt{\frac{k}{\mu}} \tag{4}$$

Where μ is the reduced mass and is equal to:

$$\mu = \frac{m_1 m_2}{m_1 + m_2} \tag{5}$$

However, in Infrared Spectroscopy is common to use the spectroscopic wavenumber as a measurement unit, that is the number of waves in a length of one centimeter, having the advantage of being linear with the energy. This spectroscopic wavenumber is given by:

$$\bar{v} = \frac{1}{\lambda} = \frac{v}{c}[=]cm^{-1} \tag{6}$$

Where c is the speed of light.

Now, in terms of spectrometric wavenumber, the vibrational frequency is given by:

$$\bar{v} = \frac{1}{2\pi c}\sqrt{\frac{k(m_1 + m_2)}{m_1 m_2}} \tag{7}$$

This vibrational frequency, on infrared-active molecules, can produce changes in bond length, like stretching or changes in bond angle, as bending. In the simplest system, the first vibrational mode can be in-phase and out-of-phase[11]. This stretching can be symmetric and asymmetric, respectively. Bending vibration can be dived in in-plane and out-of-plane bending vibration. In-plane bending vibration exists the possibility of scissoring and rocking movement as a respond of the IR absorption[11]. Movements as wagging and twisting correspond to out-of-plane bending vibration.

In summary, to generate these vibrational modes is necessary that molecule probe absorbs some part of the energy of incident IR radiation, present an electric dipole moment and change it after this absorption process[9]. Equation 8 demonstrates the relation between the intensity of incident radiation and the intensity of the radiation leaving the sample.

$$A = \log\left(\frac{l_o}{l}\right) \tag{8}$$

However, traditionally, the IR measurements are given in terms of transmittance percentage and we can obtain it from the absorbance.

$$\%T = \left(\frac{l}{l_o}\right)100 \tag{9}$$

$$A = \log\left(\frac{1}{T}\right) \tag{10}$$

$$A = -\log(T) \tag{11}$$

$$\%T = [\text{antilog}(-A)]100 \tag{12}$$

Furthermore, for IR analysis, the state-of-the-art divides this IR region into three parts. Near-IR is the first part of the IR region is around 12,820 cm^{-1} to 4000 cm^{-1} Mid-IR is between 4000 cm^{-1} to 400 cm^{-1}and Far-IR is between 400 cm^{-1} to 30 cm^{-1}. These regions excite different vibrational modes in the samples and provide more molecule information. For Near-IR is often used to elucidate overtone bands and the Far-IR is typically used for observing molecule vibration containing metal atoms, molecular skeleton vibrations, and some crystal lattice vibrations[12].

However, normally, is used the mid-IR for molecule analysis because can elucidate the simplest six characteristic vibrational states of samples and observe the fingerprint of the molecule probe, a zone that all vibrational modes are characteristic and unique for that molecule and, usually, contains a very complicated series of absorptions. These are mainly due to all manner of bending vibrations within the molecule.

While the Infrared Spectroscopy can be used as a quantify technique, its principal use is for elucidating molecular structures. However, is necessary to use another complementary technique for complete molecular structural analysis. For all that, this spectroscopy is widely used for its facile operation, fast analysis time and low-cost analysis.

1.1.2. Raman Spectroscopy

This vibrational spectroscopy is based on the detection of inelastic scattering of light produced by the interaction between a molecule probe and an incident electromagnetic radiation. This phenomenon was observed and studied by Sir Chandrasekhara Venkata Raman, being awarded by Nobel Prize in physics in 1930[13], describing this inelastic scattering effect as “its feebleness in comparison with the ordinary scattering”[14].

This inelastic scattering or Raman scattering occurs when a photon excites a molecule, promoting to ground state to a virtual energy state, producing different vibration modes due to an energy absorption process. When these molecules are relaxing, the molecule energy ends in a vibrational state, producing a photon with low frequency, in comparison with the incident photon. This process is called Stokes scattering[8].

On the other hand, an Anti-stokes scattering occurs when molecules are already in a state of greater energy and interact with an incident photon, the relaxing process leading until at molecule ground states, the photon produced after this process has a bigger frequency than the incident photon[8]. However, this phenomenon has a low probability to occur than the Stokes-Scattering according to the Boltzmann distribution[15]. These scattering processes are representing in Figure 4.

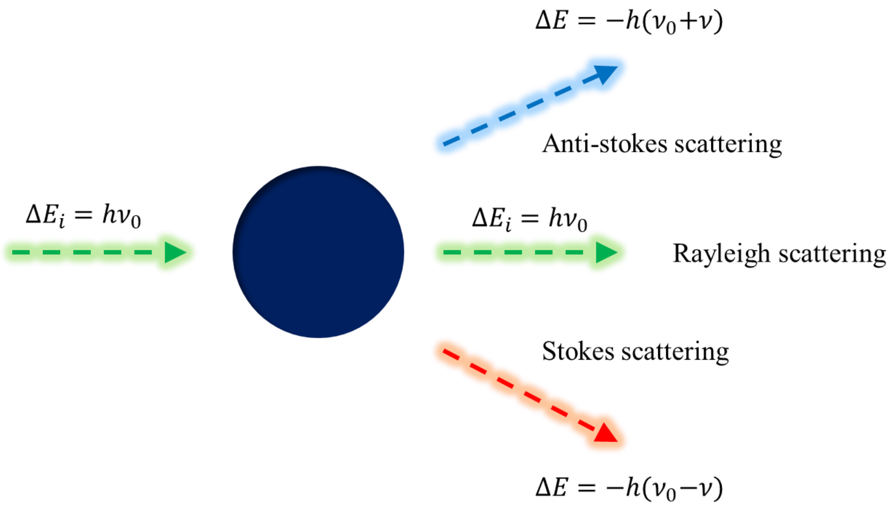

Figure 4. Different scattering processes.

For all that occurs, according to electrodynamic theory, is necessary a change in the molecule polarizability (α), exhibiting a change in the molecule electron cloud, inducing an electric dipole moment P, according to the equation 14.

$$\vec{P}= \tilde{\alpha}\vec{E} \qquad (13)$$

When an oscillating electric field distorting an electric density of a molecule, an oscillating electric dipole moment is induced,

$$E = E_0 \cos(2\pi\nu t) \qquad (14)$$

$$P = \alpha E_0 \cos(2\pi\nu t) \qquad (15)$$

Otherwise, the electric dipole moment be composed of constant vibrational movements as we can see in equation 16.

$$\alpha = \alpha_0 + \frac{\partial\alpha}{\partial Q} + \cdots \qquad (16)$$

Where α_0 is the static state polarizability and the second term is a correction due to the vibrational state. Likewise, Q *and* $Q_{0}0$ are the vibrational normal coordinate and the highest position that the molecules can be, respectively. Also, we can calculate Q as,

$$Q = \ Q_0 \cos(2\pi\nu_{vib}t) \tag{17}$$

Where v_{vib} is the vibration frequency of the molecule, that is different than the incident electromagnetic radiation frequency. Hence,

$$\alpha = \alpha_0 + \frac{\partial\alpha}{\partial Q} Q_0 \cos(2\pi\nu_{vib}t) \tag{18}$$

$$P = \alpha_0 E_0 \cos(2\pi\nu t) + \frac{\partial\alpha}{\partial Q} Q_0 \cos(2\pi\nu_{vib}t) \tag{19}$$

Resolving the equation to,

$$P = \alpha_0 E_0 \cos(2\pi\upsilon t) + \frac{\partial\alpha}{\partial Q} \frac{Q_0 E_0}{2} [\cos(2\pi(\nu - \nu_{vib})t) + \cos(2\pi(\nu + \nu_{vib})t)] \tag{20}$$

Where the first term represents the electric dipole moment induced by the Rayleigh scattering, that is a light scattering without changes in the frequency.

The other two terms represent the Stokes-scattering and Anti-stokes scattering contributions to the dipole moment at the end of the process.

Regarding of Raman intensity, this can be defined as the product of the collected and incident polarization of the radiation detected and the polarizability tensor.

$$I \propto \left|\vec{E}_s \cdot \tilde{\alpha} \cdot \vec{E}_l\right|^2 \tag{21}$$

However, the detector usually cannot be replaced or changed, the Raman intensity could be inversely proportional to the wavelength of the laser.

$$I \propto \frac{1}{\lambda^4} = \lambda^{-4} \tag{22}$$

As in Infrared spectroscopy, in Raman spectroscopy is important to consider the wavelength of the lasers to improve the Raman intensity and to decrease another signal as fluorescence that can be measured. Typically, 532, 633, 785 and 1064 nm lasers are the most employed. Nowadays, this VS is employed for different types of analysis due to its versatility and fast analysis. Pesticides[16], dyes[17], biological samples[18] and inorganic compounds[19] are an example of Raman spectroscopy application. However, in this technique, the intensities detected are very low, hindering the sample quantification.

Summarizing, the slight difference between Infrared and Raman spectroscopy regarding on the modification the permanent dipole moment and the deformability of the electron cloud of a molecule, respectively. However, the difficult to analyze in trace levels is one of the principal problems. To try improving this, the modified vibrational spectroscopies emerged. These news VS are called Surfaces-Enhanced Vibrational Spectroscopies (SEVS).

1.2. Surface-Enhanced Vibrational Spectroscopies

In the decade of 70s, a new matter-light interaction was observed. Firstly, McQuillan *et al.*[20] observed an increase in the Raman intensities due to the use of a silver electrode substrate. Then, in the same decade, Van Duyne *et al.* reported a mathematical explication of this Raman intensities increment[21].

On the other hand, in 1980 another signal enhancement was observed, but now in Infrared signal. Hartstein *et al.* observed that when a molecule interacts with IR radiation very near at a metallic surface, their IR signal increased[22]. This same phenomenon was observed and corroborated by Hatta two years later[23]. These discoveries permitted the develop of Surface-Enhanced Raman Spectroscopy (SERS) and Surface-Enhanced Infrared Absorption Spectroscopy (SEIRAS).

In both cases, the use of a metallic nanostructured surface as a substrate is necessary to generate these enhancements. Nobel metal nanoparticles as silver and gold nanoparticles are typically used as SEVS substrates due to their optical properties, because at this scale the interaction between light and the metallic nanoparticle is different. The valence electrons on the metallic nanoparticle interact with the electric component of the incident electromagnetic radiation, entering in a coherent oscillation between them. At this quantum of this electron oscillation is called plasmon. Furthermore, due to this oscillation or resonance occurs on the nanoparticle surfaces, at this phenomenon is known as Located Surfaces Plasmon Resonance (LSPR).

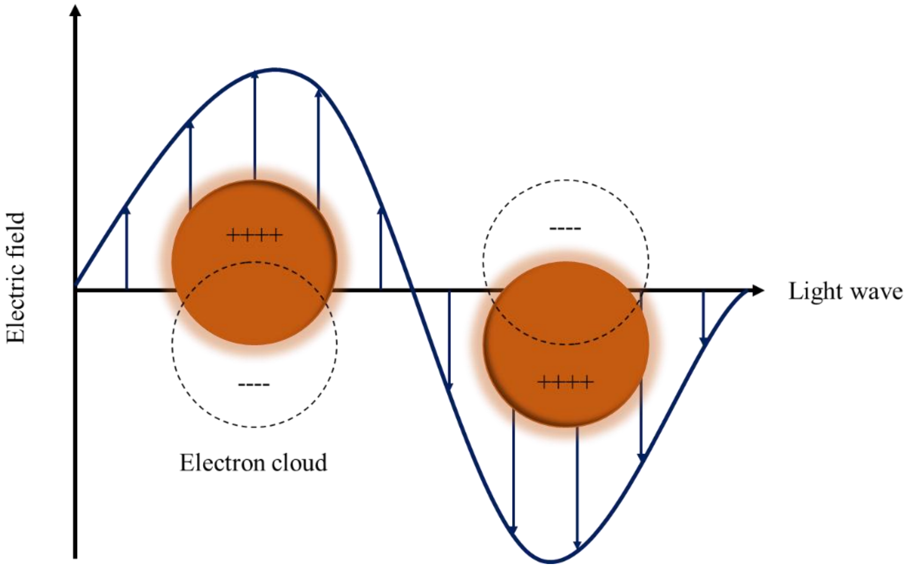

Figure 5. Located surface plasmon resonance of a noble metal nanoparticle.

On the other hand, nowadays is in constant discuss the mechanism that controls this enhancement in SEVS. One mechanism is based on the chemical interaction between the molecule probe and the SEVS substrate. This Chemical enhancement is less probably that occurs due to the chemical nature of the substrates do not allow a chemical reaction with the sample. Only some condition is possible, but for this reason, the Electromagnetic Enhancement is the actual mechanism accepted. On the following section, we will discuss it.

1.2.1. Electromagnetic Enhancement Mechanism

In contrast with the Chemical Enhancement Mechanism, in Electro Enhancement Mechanism is not necessary a chemisorption process. This mechanism consists of a re-irradiation process due to a plasmonic interaction between the plasmonic nanoparticle, the analyte, and the incident electromagnetic radiation. This process was proposed and described by Guillot in 2012 for Raman enhancements. However, this mechanism also describes IR enhancement[24,25].

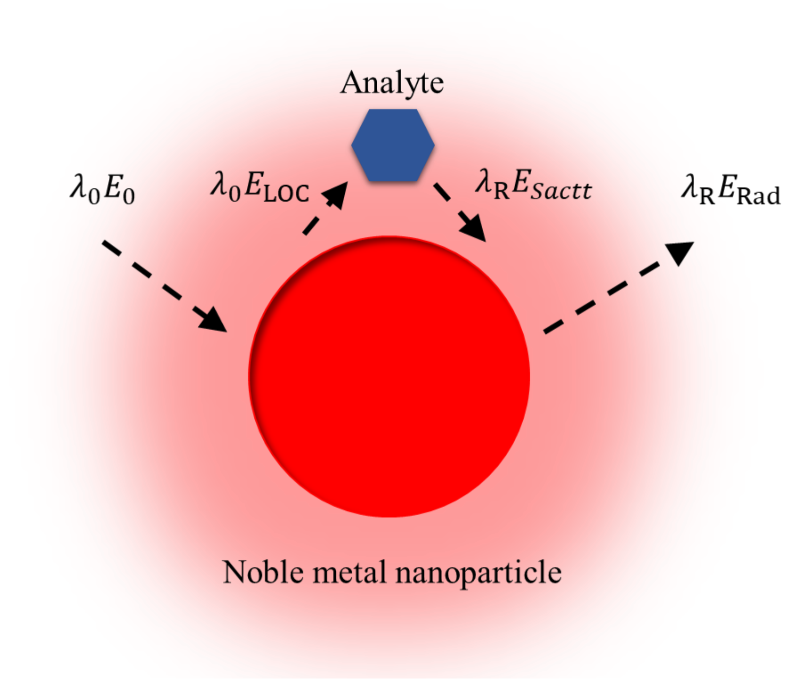

Figure 6. Re-radiation process.

$$E_{LOC} = M_{LOC} \lambda_0 E_0 \tag{23}$$

As we can see in Figure 6, when an electromagnetic radiation with an initial electric field, E_0 and wavelength λ_0, produce an enhancement on local electric field, $E_{LOC},$ due to their plasmonic interaction with the incident radiation, around the metallic nanoparticle. However, when the analyte is near to the metallic nanoparticle, the local field polarize the molecule and a Raman effect is produced. Then, this electric field of the scattered radiation can be calculated.

$$E_{scatt} = \alpha E_{LOC} \tag{24}$$

Where, E_{scatt} is the scattered electric field, α is the polarizability of the molecule, being this new produced electric field proportionally at these two components. Then, this scattered electric field interacts with the metallic nanoparticle again, producing a radiated electric field.

$$E_{Rad} = M_{Rad}\lambda_R E_{scatt} \tag{25}$$

Then,

$$E_{SERS} = E_{Rad} = \alpha M_{LOC}\lambda_0 M_{Rad}\lambda_R E_0 \tag{26}$$

Where, M_{LOC} and M_{Rad} are the located enhancement factor and radiated enhancement factor, respectively. Otherwise, the SERS intensity is proportional to these enhancement factors, as we can see in equation 27.

$$I_{SERS} = M_{LOC}^2\lambda_0 M_{Rad}^2\lambda_R I_0 \tag{27}$$

Besides, as the Raman-shifted and incident wavelength have almost the same value, we can express the SERS intensity as,

$$I_{SERS} \approx M_{LOC}^{4} \lambda_0 I_0 \qquad (28)$$

While in SERS, the intensity can be fourth-power enhanced; in SEIRAS, the electromagnetic enhancement on the local electric field of the metallic nanoparticle substrate surfaces is proportional to the square of the local electric field.

$$I_{SEIRAS} \approx M_{LOC}^{2} \lambda_0 I_0 \qquad (29)$$

However, for that phenomenon occurs is almost necessary that the vibration of the permanent dipoles of the molecules is found inside of a nanogap between two metallic nanoparticles, where the electric field increase, called hotspot[26]. Also, SERS is beneficiated by hotspot and, for it develops, the obtention of metallic nanostructured substrates are essential for developing SEVS techniques[27].

1.2.2. SEVS Substrates

Chemical and physical methods have been developed for SEVS substrate obtainment[28] for control the number of the hotspot on the substrate. All these methods are based on the assembly of noble metal nanoparticles as Ag or Au nanoparticles due to their optical proprieties and widely use on SEVS.

Physical methods control the assembly at the nanoscale with high precision, developing tidy arrangements of noble metal nanostructures on the surface of the substrate[29]. However, this kind of methods is highly expensive, preferring the chemical methods for their easy application and fast obtention of SEVS substrates.

Chemical methods are based on the chemical reaction on the substrate surface[30]. When noble metal nanoparticle formation occurs on the surfaces of the substrate, these are deposit immediately, obtaining the correspondent noble metal SEVS substrate. However, this fast assembly produces poor tidy nanostructured arrangements, obtaining a low reproducibility on the hotspot formation.

On the other hand, different morphologies of noble metal nanoparticles are preferred for SEVS substrates. When some regions as edges or spikes are joined, increase the local field between them, creating hotspots[31]. However, to control their size and shape is hard to reproduce, obtaining variations on their monodispersity and to try to perform it, a new emerged scientific field propose novel strategies to synthesis and assembly of noble metal nanoparticles for SEVS substrates. This scientific field is named Microfluidics.

1.3. Microfluidics

Although the study of fluid behavior at small scales began in 1960[32], it was not until 2006 when Professor George M. Whitesides published his revolutionary article entitled *The origins and the future of microfluidics* where defined the science and technology of the process of manipulating small (10^{-9} to 10^{-18} liters) amounts of fluids, using channels with dimensions of tens to hundreds of micrometers, as microfluidics[33].

When fluids are confined at these dimensions and manipulated at this scale, other parameters govern their behavior. Mainly, on these conditions, the fluid behavior is determined by dimensionless numbers that describe the competition between buoyancy, gravity, inertia, viscosity and interfacial forces, being the Reynold number, Re a parameter for predict the flow pattern[34].

$$Re = \frac{\rho U D_H}{\mu} \qquad (30)$$

As we can see in equation 28, Reynold number compare the inertial force with the viscous force of the fluid. Where U is the velocity of the fluid, D_H is the hydraulic diameter of the microchannel, μ is the viscosity and, ρ is the density of the fluid, describing that when viscous force is dominant over the inertial force, a control on the fluid occurs producing a smooth movement on layers that is called laminar flow.

The capillary number is another dimensionless number that describes the reduction on the gravitational effect when viscous stress and capillary pressure increase due to the reduction on the microfluidic device length. This number is inversely proportional to interfacial tension[35]. Equation 29 describes the capillary number, Ca where, γ is the interfacial tension.

$$Ca = \frac{\mu U}{\gamma} \tag{31}$$

Otherwise, when inertial and capillary forces are dominates in comparison with viscous stress, Webber number could be an important dimensionless number[36].

$$We = Re \cdot Ca = \frac{\rho D_H U^2}{\gamma} \tag{32}$$

On the other hand, when a fluid presents a laminar flow (Re <2000) diffusion transport mechanism dominates. This occurs when exist a molecular concentration gradient through the fluid, moving from the most concentrated area to the less concentrated zone caused by the increase in the entropy of the system. However, if the system is altered by an external force as heating or mixing, convection and migration can be a dominate transport mechanisms[37].

Furthermore, when an existing relation between diffusion and flow rate, we can study different flow situations using another dimensionless number named Peclét number.

$$Pe = \frac{UL}{D} \tag{33}$$

Where L is the length of the microchannel and D is the diffusion coefficient, describing when diffusion has a minor influence on the system, molecules flow according to the externally applied driving force. Besides, this number with Reynolds number predicts the flow phenomenon that governs on the fluid system, being important the prediction of each system to apply using microfluidics and, thus can design correct microfluidic devices according to the needs[38].

1.3.1. Microfluidic Devices

A microfluidic device is a tool capable to enclose the fluid at the microscale and make flow it through microchannels at different flow rates as such require. The design and material conformation of microfluidic devices are strongly depending on their application. However, fluid behavior is related to the flow regime and, for control, this is necessary to consider the flow pattern[34].

Continuous flow and segmented flow are the most applied flow patterns, where in the first one, the fluid velocity is related to the boundary conditions producing a parabolic distribution. Besides, a diffusion transport mechanism governs due to the absence of turbulence. This flow pattern does not require a complex design device[39].

However, in segmented flow is necessary to consider a join between microchannels and between continuous and dispersed phase. T-junction[40], flow-focusing[41] and co-flowing[42] microfluidic devices are an example of microfluidic design. On T-junction, the dispersed phase is entered to the side channel, and the continuous phase is injected into the main channel, producing monodisperse droplets. Also, in flow-focusing, an immiscible phase cut the continuous phase, focused it into a smaller microchannel creating a thin jet with an elongation-dominated velocity. This jet ends up breaking into small drops. Finally, co-flowing is composed of a concentric capillary, in a coaxial direction. The continuous phase and dispersed phase are individually injected through each capillary, forming a parallel flow. In this regime, the disperse phase becomes unstable due to the interfacial force, decreasing the interfacial area. This results in the breakup of the disperse phase into droplets.

1.3.2. Microfluidic Synthesis and Assembly

As we have seen, microfluidics promises a better control in the different transport mechanisms and, whatever the flow pattern to be used, the use of less volume would allow focused synthesis without energy waste, favoring its reproducibility, where the nanomaterials produced in batch conditions could be replicated with an excellent control in size distribution, shape, and composition[43].

With the help of microfluidics, the mechanisms that dominate the formation of nanomaterials, as noble metal nanoparticles, can be controlled. The control in the LaMer mechanism, Ostwald ripening, Finke-Watzky mechanism and coalescence, and oriented attachment would allow the nanoparticle synthesis, including the assembly of noble metal nanoparticles, favoring the obtaining of SEVS substrates[34,39].

For all these fundamentals, in this manuscript, we report the advances on the study of microfluidic synthesis and assembly of noble metal nanoparticles for the to develop of SEVS substrates to try copulin microfluidics with SEVS for improving its efficiencies.

CHAPTER II

BACKGROUND

In 2018, Fikiet M. *et al*.[44] reported a review article, where expose the most recent application of SERS in security trends. They talk about biological samples[45], controlled substances and toxicology[46], explosives and gunshot residues[47] and trace analysis in paints[48] and fibers[49].

However, it is important to highlight the detection of controlled substances and toxicological applications of SERS had they report. As we know, SERS is used for the identification of illicit drugs and metabolites in body fluids at real-time. In this report, they show that it is possible sensing cathinone (illegal amphetamine derivative) through SERS, corroborating that SERS is an effective technique for the detection of this drug in a concentration range of 10^{-10} – 10^{-12} $molL^{-1}$ [46].

Furthermore, they report the use of SERS for explosives and gunshot residues detection, emphasizing the importance of SERS as analytical tool in terms of security. In this field, it is preferable the application of selective and sensitive techniques because this kind of samples can compromise the health of the analyst and can be easily contaminated.

In the same way, SERS has had a widely application on Healthcare field. As we can see on the reported work by Li M. *et al.*[50].In this year, they used an Au nanoparticle SERS substrate with antibody modified surface for cancer detection on human breast cells. Also, with this SERS nanoprobes, they could obtain multicolor images for these cancer cells at $3.33x10^{-11}$ $molL^{-1}$. This example provides that with the use of a SEVS technique as SERS is possible to design new strategies for cancer detection in a fast and easy manner.

Another SERS application is on pesticides residues detection. For example, in this year Yaseen T. *et al.*[51] exposed an effective SERS analysis to simultaneously detect of multi-class pesticide residues such as thiacloprid, profenofos and oxamyl in standard solution and peach fruit extract, using Au@Ag core-shell nanoparticle SERS substrate. They achieved limits of detections (LOD) as low as 0.1 mg/kg for thiacloprid and 0.01 mg/kg for both profenofos and oxamyl pesticides in peach extract. However, this method that they developed is limited at bigger concentration of analytes, being difficult to realize SERS analysis in trace levels for pesticides residues in fruits extracts. Therefore, this methodology could be a potential candidate in environmental and food safety.

As we can see, one of the most important factors for the enhancement of the signal in different SEVS is the substrate[52]. These substrates are making with different materials, like metal oxide and/or noble metal nanoparticles, which each one of them provides their properties and produce a signal enhancement[53].

There are different reports that show several substrate fabrication methods and their diverse SEVS applications. In 2017, Wenbing Li *et al*.[28] reported a review article where they expose several substrate fabrication techniques with respect to noble metal SERS substrates. Also, they divide them into big groups according to the physical and chemical methods. These groups are solid-state SERS substrates and manufactured substrates through chemical synthesis.

For the first group, one of the most used fabrication methods is the electron beam lithography (EBL). This method consists of a top-down construction, where using an electron beam, is possible to devastate a material in the order of nanometers. Also, this method permits to produce reproducible gaps between nanoparticles[54]. Another method in this group is the film over nanosphere (FON), which consists of evaporation of a thin noble metallic film on polystyrene nanospheres[55]. Also, they show a thermal method that consists in obtaining hybrid materials between noble metal nanoparticles and another metal nanoparticle or metal oxide nanoparticle[56].

Besides, as we mentioned, they also report different chemical methods as self-assembly and its variations[57], chemical, and photochemical synthesis[53], among other methods. In contrast with the physical methods, chemical methods consist of the down-to-up construction of the substrates. For example, in the self-assembling method is common the use of reducing or precipitant reactants for the metal nanoparticle obtainment from its metallic ions[58]. Also, they say that it is possible to use a facile and greener mechanism for the metal or noble metal nanoparticle production. For example, in a photochemical synthesis we can use light irradiation for the reduction of metallic ions into nanoparticles[59].

Furthermore, another widely applied SEVS is surface-enhanced infrared absorption spectroscopy also needs the correct preparation of substrates for its appropriated performance. In 2018, López-Lorente A. I. *et al*.[60] published a paper where describe the preparation of different SERS and SEIRAS metal oxide substrates. In their work, they prepared distinct SERS and SEIRAS substrates based on Ag and TiO_x/ZnO nanoparticles via top-down ion beam sputtering deposition on silicon substrates and they concluded that it is possible to obtain signal enhancements in both SEVS techniques.

As we can see, there are several methods and techniques for substrate preparation, but these are very expensive or do not produce substrates with high reproducibility. One opportunity to try reducing costs and increase the substrate reproducibility is the recently explored scientific field called microfluidics. With this knowledge, it is possible to simulate and control different discrete systems at microscale for noble metal nanoparticle synthesis[61].

There are many papers about microfluidic synthesis of noble metal nanoparticles today. For example, Lawanstiend D. *et al*.[62] in 2019, synthesized Ag microstructures by a microfluidic synthesis for SERS applications. They designed a polydimethylsiloxane (PDMS) microfluidic device with three inlets and one outlet, where the channels dimensions were 300 and 100 µm deep. The size of the entire device is 2 cm. In the channels, they flowed NaCl and $[Ag(NH_3)_2]^+$ to make them converge and start the reaction. They obtained AgCl is used as a template and generates the Ag microstructures. Also, they proved different condition and reducing agents as flow rate and $NaBH_4$ and how this condition generates morphological differences. They used all these nanoparticles obtained as noble metal SERS substrates for SCN^- detection in human saliva, concluding that it is realizable to obtain a Raman signal enhancement and high reproducibility using these substrates.

Furthermore, this year, Abalde-Cela S. *et al*.[63] reported the microfluidic synthesis of Au nanoparticles with high control of size and shape. They compared this synthesis with a bulk synthesis. Also, they worked with two different conditions, with and without surfactant, for the Au nanoparticle preparation. The nature of each kind of synthesis forced to develop different microfluidic devices. For the surfactant-based synthesis, they prepared a microreactor with five inlets, two mixers and one outlet, where flowed oil and surfactant, polyvinylpyrrolidone and $HAuCl_4$ and Au seeds are connected to the inlets, and they collected the Au nanoparticles in the outlet. For the free-surfactant synthesis, they fabricated a microreactor with six inlets, three mixers, and one outlet, where they flowed oil, $HAuCl_4$, HCl, Au seeds, $AgNO_3$, and ascorbic acid on the inlets. Like the previous microreactor, they collected the Au nanoparticles in the outlet. It is important to note that they fabricated both microfluidic devices with the same technique. They used PDSM as material by soft photolithography, generated 120 μm x 75 μm as dimensions of the channels. Also, some T-junctions were of 80 μm x 75 μm.

They proved that it is possible to obtain Au nanoparticles with higher shape control and narrow size distribution. These qualities are not able to obtain through bulk synthesis methods. Moreover, with this condition, is viable to obtain the same results over and over. Also, this synthesis is being applied for fabrication of SEVS substrates due to the reproducibility of the synthesis.

On the other hand, in 2019, Huang H. *et al*.[64] synthesized Au nanoparticles without capping agents using CO as reducing agent, producing nanoparticles with polydispersity as low as %5 using a segmented-flow glass tubing reactor. Also, they tested these Au nanoparticles on rhodamine 6g analysis using SERS and compare the obtained results with Au nanoparticles with capping agents, synthesized with the same tubing reactor, observing a lower enhancement than the Au nanoparticle without capping agents due to the Raman signal decreases exponentially with the distance between the metal surface and the molecule probe[65].

This microreactor had a helical mixer to improve the mix on the liquid slugs and improve nanoparticle monodispersity[66]. They varied the flow rate ratio of Au^{3+}/CO to control the final Au concentration and observe how affect this on nanoparticle size and shape. They observed that when the Au^{3+}/CO increases, the nanoparticle size increased, and the nanoparticles had a non-spherical morphology. Also, pH effect was measured observing a changing on nanoparticle size from 5 to 12 nanometers due to formation of nuclei and particle growth occur at the same time because the reactivity of the Au^{3+} decrease when hydroxylated species appears when the pH increase[67].

Manno R. *et al*.[68] published another example of the microfluidic versality synthesis. They, with a Teflon helical tubing reactor, synthesized Ag nanoparticles employed conventional and microwave heating. For this, they fabricated two distinct setups for each heating method. The mixer of this microreactor was rolled up on a quartz tube where the conventional heating was applied.

They studied the relation of total flow rate on the Ag nanoparticle continuous-flow synthesis in each heating method. For that, they employed $AgNO_3$ as metal precursor, polyvinylpyrrolidone as stabilizer and ethylene glycol as reducing agent and tried 0.1, 0.2, 0.3, 0.6 mL/min as flow rates, observing a bigger Ag nanoparticle using microwave heating at low flow rates due to the fast heating of on inner fluid, resulting in faster nucleation and growth.

Other example of microfluidic synthesis is the work published in 2017 by Kulkarni A. A. *et al*.[69] synthesized Au nanostructures using a segmented-flow Si/Pyrex microfluidic device. This chip was fabricated with a mixer and heater zone with 400 µm in depth and width, having a reaction volume of 100 µL. They evaluated different organic reducing agent, flow rates and temperature conditions as well as distinct surface properties on the microchannel walls to improve the mixing of the reaction slugs, being the most important contribution of this work.

Through hydrophilic microchannels, the chemical reaction started between the organic droplets of the continuous phase[70], observing important change on shape. On the other hand, when the surface property is hydrophobic, little slugs of aqueous phase contained the reactants, occurring the reaction inside of the slug or droplet, showing an important change in size[71].

As we can see, it is possible to synthesis noble metal nanoparticles with better control on their size and shape using microfluidics conditions and different microfluidic reactor conformations as PDMS/Glass devices, tubing microreactors or Si/Pyrex devices, being a good alternative to develop SEVS substrates.

However, for each microfluidic synthesis is very important to choose an appropriated device design and, depending on their requirements, to choose a suitable fabrication methodology. For this reason, it is crucial to know the different microfluidic device fabrication techniques. There are several fabrication techniques so much so that, in 2019, Gale B. *et al*.[72] reported a review article where condensed all the fabrication techniques and its diverse grouping. They describe four groups: laminates[73], molding[74], 3D printing[75] and nanofabrication[76].

Fabrication technique by laminate consists of the laminar parts obtainment and its assembly[77]. They mention three basic steps for this technique. The first step is the material selection, as PDMS, polymethyl methacrylate (PMMA), polycarbonate, and cyclic olefin copolymer (COC). Then, the next step is the cutting of desired microfluidic features in each layer using knife plotter or laser technique. The last step is the bonding of the independent layers together to form one functioning device. They mention two ways for this bonding, adhesive and thermal bonding.

The second fabrication technique is molding. Gale and their collaborators divide this group into three classes: replica molding[78], injection molding[79], and hot embossing[80].

Replica molding is based on photolithography, that consists in produce a pattern using a photomask and a photosensitive resin spread on a substrate where, depending on the resin type, is possible to generate molds[81]. These molds could be sealed with another substrate or molded using a liquid-set polymer, such as PDMS to obtain microchannels[82].

Injection molding consists of using a melted thermoplastic and then inject it into a mold cavity, then cool this mold cavity and removed it. Hot embossing using thermoplastics or polymers that become viscous liquids at elevated temperature. In this technique, a thermoplastic o polymer film its place on two molds, then it compresses and heated, creating a cast of the mold. Besides, the mold it cools, and the cast it removes. The authors emphasize, in these techniques, the low-cost production and the facile microfluidic devices fabrication.

Also, as the third fabrication technique, they explain the 3D printing as a layer-by-layer manufacturing technology, in which a new layer of material it adds on top of the previous layer[83]. In this review, they are described four classes of 3D printing: fused deposition modeling (FDM)[84], stereolithography (SL)[85], multi-jet modeling[86], and two-photon polymerization[87]; highlighting the first one because is the most common extrusion-based method. In this technique, a material it melts and then it extrudes onto the previous layer, where it binds before cooling. Also, the authors explain that this kind of techniques now are cheaper and very useful as pre-fabrication technique for microfluidic devices.

Finally, the last fabrication technique that they describe is nanofabrication. They mention that exist two methods for this kind of devices. Top-down methods allow for good control of the size and distribution of features, and they commonly involve some form of photolithography. Bottom-up nanofabrication techniques involve the formation of nanoscale structures through the self-arrangement of atomic and molecular building blocks. This molecular nature allows for highly repeatable periodic structures. They also examine four nanoscale methods: extreme ultraviolet[68] electron beam[88] and nanoimprint lithographies[89] and anodic aluminum oxidation[90].

However, they explain that these techniques are starting to use, but promise to be a low-cost and fast methodology for the microfluidic device fabrication. Besides, they mention that the technique par excellence until now is the soft lithography. This technique belongs to the molding methods and is the most used; however, it has a remarkable limitation as for the needed of a clean-room and expensive instruments.

For all this, the correct fabrication of a microfluidic device for different material synthesis that it can be used as SEVS substrates, would allow the fast detection analytes in complex samples. In this way, the design and fabrication of microfluidic devices for the simultaneous synthesis and assembly of noble metal nanoparticles would allow high morphological control of the SEVS substrates, which leads to a fast fabrication of reproducible SEVS substrates.

2.1. Hypothesis

Synthesis and assembly processes of noble metal nanoparticles with segmented-flow microfluidic control allows the fabrication of SEVS substrates for 4-ATP SERS detection by surface-enhanced Raman spectroscopy.

2.2. General Objective

To synthesize and assemble Au and Ag and using a microfluidic reactor for the fabrication of SEVS substrates and study of the physicochemical features related with the fabrication and performance.

2.3. Specific Objectives

- To design and fabricate a microfluidic device for the synthesis of noble metal nanoparticles.
- To synthesizes Ag and Au nanoparticles by microfluidic synthesis.
- To characterize Au and Ag obtained nanoparticles by microfluidic synthesis.

- To design and fabricate a microfluidic device for the assembly of noble metal nanoparticles.
- To assemble the obtained Ag and Au nanoparticles by microfluidic assembly.
- To characterize the Ag and Au assembled nanoparticles.
- To evaluate the performance of the substrates obtained using microfluidic synthesis and assembly in SEVS and compare them with the correspondent substrates obtained using conventional methodologies as reference.

CHAPTER III

MATERIALS AND METHODS

3.1. Design and Microfabrication of Microfluidic Devices

3.1.1. Design and Microfabrication of PDMS/glass Microfluidic Devices

For the development of these devices, SU-8 2035 resin and SU-8 developer was purchased from Microchem™. For the characterization of the molds, a mechanical profilometer was used.

Two types of segmented-flow microfluidic devices were designed using AutoCAD 2019.-Student Version software (Serial Number: 901-42327206). Also, some reference line marks for 4 inches Ø Si wafer were provided by Group 7 of the ICMCB.

The first type of microfluidic device was design with 55 mm in width and 21 mm in length. This microfluidic device had 3 inlets and 1 outlet, each one with 1.2 mm Ø. A bottleneck was designed as a segmented-flow requirement with 0.1 mm in width and 0.1 mm in length. Also, a serpentine-tube mixer was designed with rounded corners and 0.02 mm in width and 18 mm in length. This design was done twice until the reference mask limits to complete the space of the reference mask.

The second type of microfluidic device was design with the same first design specification for inlets, outlets and microchannels in width. However, to improve the residence time and sample manipulation, this design had 55 mm in width and 64 mm in length, as dimensions. Once the designs were obtained, the masks were sent to print.

To microfabricate the previous microfluidic devices designs, we employed the ICMCB Group 7 procedure[91]. In addition, all procedure was elaborated inside cleanroom. Figure 7 shows the step-by-step procedure of PDMS/glass devices microfabrication.

For the development of a master mold, a 4 inches Ø Si wafer with 1000 µm ± 25 µm was used as substrate and SU-8 2035 as negative photoresist resin. For this, 4 mL of SU-8 2035 was poured on the pre-cleaned silicon wafer and then spin-coated it at 500 rpm during 10 s and, for second time, at 2000 rpm during 45 s (Figure 7a and b). Then, a soft bake at 80 °C during 30 min was applied. A second resin deposition was realized at 500 rpm during 10 s and then at 3000 rpm for 45 s and soft-baked at 80 °C during 40 min.

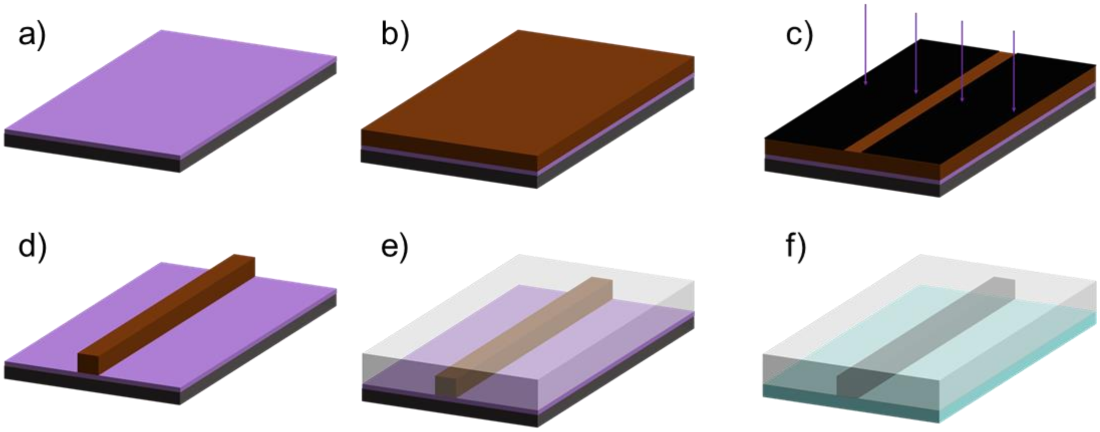

Figure 7. Step-by-step procedure of PDMS/glass device microfabrication. A) 4 inches Ø Si wafer. B) Deposition of SU-8 2035 negative photoresist resin. C) UV print of mask design on the resin. D) Resin development with SU-8 developer. E) Molding of the master mold with PDMS. F) PDMS/glass bonding.

After the resin deposition, a UV insolation at 40 mJ/cm^2/s during 11 s was applied, aligning the printed mask with the Si wafer and then, another soft bake was realized at 85 °C for15 min. After this, the resin was developed using SU-8 developer, obtaining the mask pattern (Figure 7c and d).

To prepare the polydimethylsiloxane (PDMS), silicone elastomer was and curing agent were mixed at 10:1. After mixing, the bubbles formed into the PDMS was evacuated using a vacuum system. Then, a surface silanization of the resin was made by vacuum evaporation of the octadecyltrichlorosilaneperfluoro. Finally, the PDMS was poured on the silicon wafer mold and then, was heated (Figure 7e).

When the PDMS part was obtained, an air-plasma treatment was applied on PDMS and microscope glass slide surfaces to generate an irreversible bonding between each part, obtaining PDMS/glass devices (Figure 7f). Is important highlight that the inlets and outlets was punctured before the PDMS/glass bonding.

3.1.3. Design and Microfabrication of Microfluidic Tubing Reactor

A co-flow tubing reactor was fabricated using a translucent PTFE tubing with I.D. 0.762 mm and O.D. 3.175 mm as mean tube and two SiO_2 capillaries with I.D. 100 μm and O.D. 200 μm Ø were used as inlets, which were connected by using a Y-shape Tee with bore hole diameters of 300 μm. The silica capillaries are connected to the Tee by the mean of short flangeless PEEK fittings and simple tubing sleeves, whose internal diameters match the external diameters of the capillaries.

In addition, a Tee connection was placed downstream allowing the injection of the carrier fluid (silicon oil) and the creation of droplets-based flow. Figure 8 shows the final concept of design of the tubing reactor.

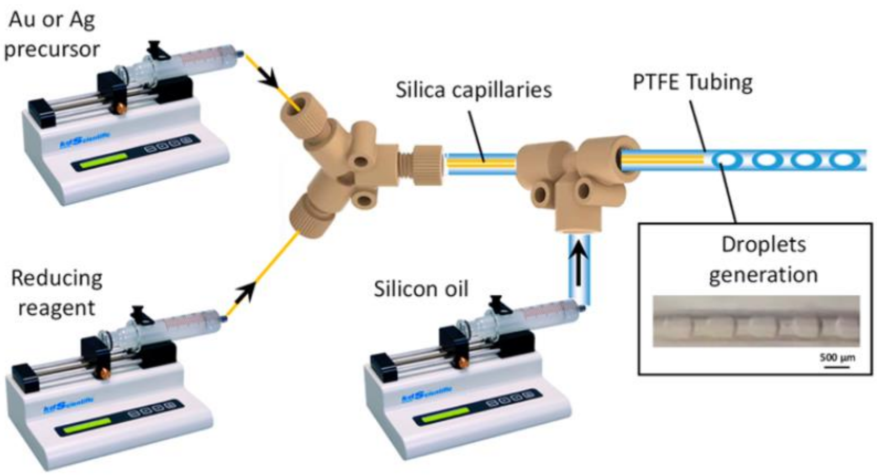

Figure 8. Scheme of tubing reactor employed for microfluidic synthesis of noble metal nanoparticles.

The tubing length downstream the droplets generation point was adjusted depending on the metal nanoparticles synthesis process.1 m (0.46 mL volume) and 1.9 m (0.87 mL volume) long for the Ag and the Au NPs synthesis, respectively.

3.2. Microfluidic Synthesis of Noble Metal Nanoparticles

All the chemicals were purchased from Sigma Aldrich. $AgNO_3$ and $AuHCl_4 \cdot 3H_2O$ were used as metal precursors for each synthesis, and $NaBH_4$ as well as Na_3Cit were employed as reducing agent on Ag and Au synthesis, respectively. On the other hand, all solution was prepared with 18.2 $M\Omega cm^{-1}$ MilliQ water.

In all microfluidic reactors, the reagent solutions were pumped with KDS100 syringe pumps from KD Scientific™, counting with three; one for continuous phase silicone oil (10 cSt @ 25 °C) and two for the Ag and Au precursors. The pumps were equipped with 5 mL SGE™ glass syringes.

For Ag synthesis one syringe contained 1 mL of MilliQ water, 3 mL of Na_3Cit 5 mM and 1 mL of $AgNO_3$ 1mM and the other syringe contained 5 mL of $NaBH_4$ 8 mM. In Au synthesis, one syringe contained 5 mL of $HAuCl_4$ 0.25 mM and the other one contained 5 mL of Na_3Cit 34.5 mM. The flow rate conditions were changed depending on the residence time required.

The droplet formation and segmented flow stability was monitored using an optical stereoscope. The nanoparticles obtained was optical and morphological characterized by UV-Vis spectrophotometer Agilent CARY 5000 and Transmission Electron Microscopy JEOL JEM2 2100 LaB_6 200 kV, respectively.

3.2.1. Microfluidic Ag Nanoparticles Synthesis

The Ag and Au NPs synthesis conditions, employed in the further sections were chosen after several experimentations and observations founded in Appendix B.

3.2.1.1 PDMS/glass Microfluidic Device

Ag NPs microfluidic synthesis was carried out flowing the aqueous phase at 0.08 mL/h and the continuous phase at 0.12 mL/h with Span 80 at 0.3% wt., at 0.35 mL/h.

The product was collected after waiting, at least, the equivalent of three residence times and the droplet formation was followed using an optical microscope.

3.2.1.2. Microfluidic Tubing Reactor

Ag NPs were synthesized at two different residence times, 0.6 (sand 3 min (Ag-1 and Ag-2, respectively). Table 1 shows the flow rate condition used. These experiments were carried out without surfactant. The samples obtained were optical and morphological characterized by UV-Vis and TEM.

Table 1. Flow rate conditions for Ag nanoparticles synthesis.

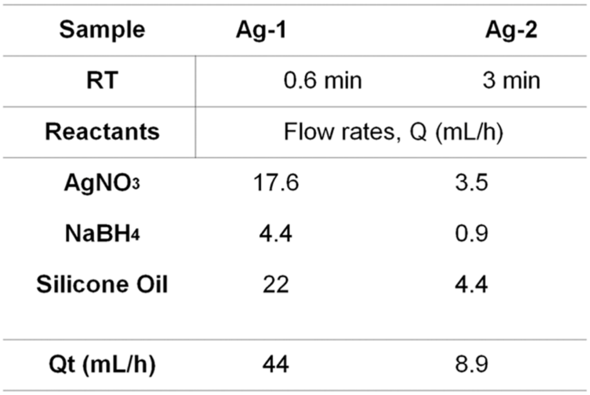

Sample	**Ag-1**	**Ag-2**
RT	0.6 min	3 min
Reactants	Flow rates, Q (mL/h)	
$AgNO_3$	17.6	3.5
$NaBH_4$	4.4	0.9
Silicone Oil	22	4.4
Qt (mL/h)	44	8.9

3.2.2. Microfluidic Au Nanospheres Synthesis

3.2.2.1 Microfluidic tubing reactor

Au NPs were synthesized using the Turkevich method adapted to flow conditions. To proceed with this method, the PTFE tubing was coiled and immersed in an oil bath heated at 105 °C. Four different residence times were employed at 3, 5, 10 and 20 min (samples Au-1, Au-2, Au- 3 and Au-4, respectively). Table 2 shows the conditions used to this synthesis. The samples obtained were optical and morphological characterized by UV-Vis and TEM.

Table 2. Flow rate conditions for Au nanoparticles synthesis.

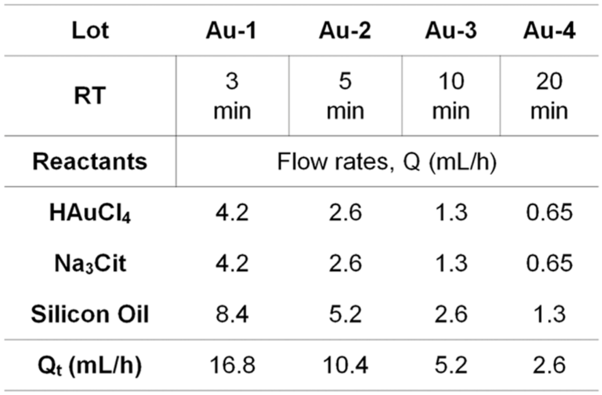

Lot	**Au-1**	**Au-2**	**Au-3**	**Au-4**
RT	3 min	5 min	10 min	20 min
Reactants	Flow rates, Q (mL/h)			
$HAuCl_4$	4.2	2.6	1.3	0.65
Na_3Cit	4.2	2.6	1.3	0.65
Silicon Oil	8.4	5.2	2.6	1.3
Q_t (mL/h)	16.8	10.4	5.2	2.6

3.3. Microfluidics and Surface Enhanced Raman Spectroscopy

3.3.1. Design and Microfabrication of Si/Pyrex Microfluidic Devices

For SERS analysis using microfluidic devices, three different design of Si/Pyrex microfluidic devices were designed and microfabricated. S1818 resin and MF-319 developer was purchased and employed from Microchem™.

Three types of segmented-flow microfluidic devices were designed using AutoCAD 2019.-Student Version software (Serial Number: 901-42327206). Also, some reference line marks for 4 inches Ø Si wafer were provided by Group 7 of the ICMCB.

The microfabrication was carried out following the ICMCB Group 7 Si/Pyrex procedure. In addition, all procedure was elaborated inside cleanroom. Figure 9 show the step-by-step procedure of Si/Pyrex devices microfabrication.

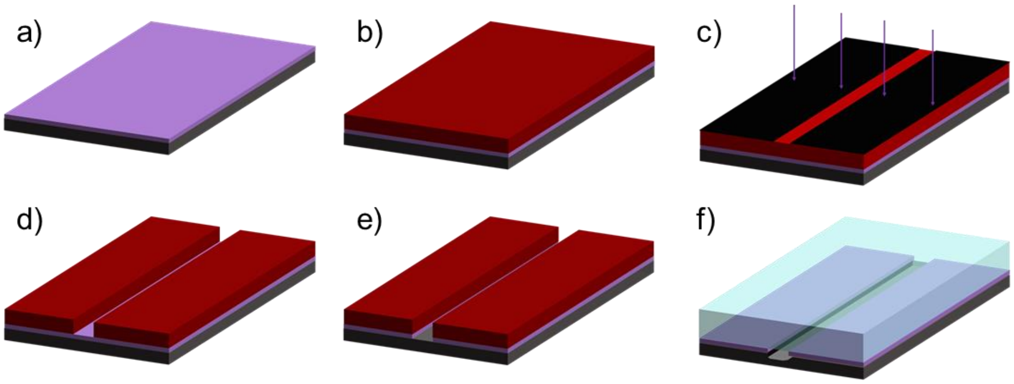

Figure 9. Step-by-step procedure of Si/Pyrex device microfabrication. a) 4 inches Ø Si wafer. b) Deposition of S1818 positive photoresist resin. c) UV print of mask design on the resin. d) Resin development with MF-319 developer. e) TMAH chemical attack on Si surface. f) Si/Pyrex anodic bonding.

First, a 4 inches Ø Si wafer with 1000 µm ± 25 µm was cleaned with isopropanol and ethanol, then was dried with compressed air. After that, ¾ of the Si wafer diameter was covered with S1818, the positive photoresist resin. Then, 1200 rpm during 30 s were applied for coating all the wafer surface. After spin-coating process, the Si wafer was placed on a hot plate at 115 °C for 4 min (Figure 9b).

For the photolithography process, the printed mask was aligned and then, a UV isolation was applied during 45 s at the same conditions using in the PDMS/glass devices procedure. After this, the Si wafer was dipped in MF-319 developer for 30 s and washed with MilliQ water. Then, the wafer was placed on a hot plate at 115 °C during 6 min (Figure 9c-d).

Then, for SiO_2 elimination, a wet etching process was developed following the health and safety group 7 rules. For this, a solution of $NH_4F \bullet HF$ 30% wt. in water was poured only on the chip regions, following the line marks. Then, the silicon wafer was rinsed with water, acetone and ethanol. Then, the wafer was submerged in a tetramethylammonium hydroxide (TMAH) solution at 90 °C. The time of submersion was adapted at the typical etching rate (30 µm/h) for try to obtain 85 µm of depth (Figure 9e). The depth of the microchannels is followed using a profilometer and, if the desired depth has not been reached yet, the procedure is repeated.

After wash with water the Si wafer, an oxidation process was performed on it. For this, the wafer was placed inside of an oven at 1000 °C with humidity condition. This condition was carried out with sprayed water using a syringe pump at 1 mL/h. The duration of the process was left overnight to ensure the full surface oxidation.

Then, on a 4 inches Ø Pyrex wafer with 1000 µm ± 10 µm of thickness, the inlets and outlets were punctured using a microdiamond drill, aligning the Pyrex wafer with the Si wafer.

For last step, an anodic bonding process was performed. Firstly, the Si wafer is submerged in Piranha solution for 5 min to eliminate all organic traces on the surface, washing with water after this. Then, the Si and Pyrex wafer were perfectly aligned to match all the inlets and outlets and pressed together to improve the bonding. After that, both wafers are carefully placed on the anodic bonding apparatus and heated until 400 °C for 1 h. Later, 250 V are applied and, once the electric current was stable, the tension was increased by 100 volts at a time until 1250 volt. When this voltage is reached it was left for 1 hour and 3 cycles are repeated (Figure 9f). After this, the Si/Pyrex wafer is cut with a precision cutter, following the line marks for obtain the individually microfluidic devices.

3.3.2. Microfluidic-SERS Analysis

To perform SERS analysis the surfaces of Si/Pyrex Microfluidic-SERS devices were functionalized by 3-MPTMS silanization process, following the flow rate and time conditions showed in Table 3.

Table 3. Flow rate and time conditions for surface silanization process.

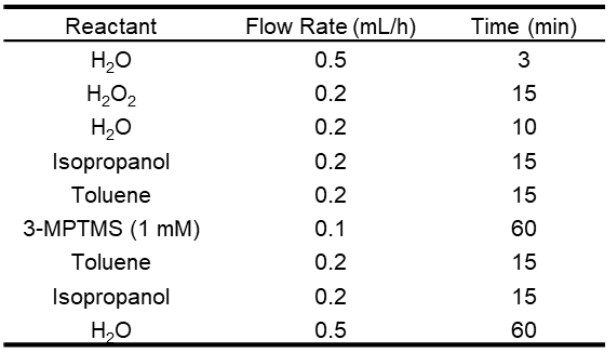

Reactant	Flow Rate (mL/h)	Time (min)
H_2O	0.5	3
H_2O_2	0.2	15
H_2O	0.2	10
Isopropanol	0.2	15
Toluene	0.2	15
3-MPTMS (1 mM)	0.1	60
Toluene	0.2	15
Isopropanol	0.2	15
H_2O	0.5	60

Once the surfaces were functionalized, the devices were loaded with Au nanoparticles previously synthesis for microfluidic SERS analysis. We flowed Au nanoparticles at 80 µL h^{-1} during 30 min. Then, different concentration of 4-ATP was flowed at 20 µL h^{-1} during 30 min. Table 4 summarize each experiment.

Table 4. Flow rate conditions of Au nanoparticles and 4-ATP for microfluidic-SERS analysis.

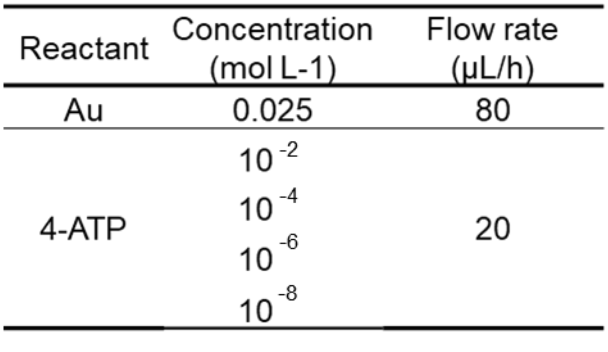

Reactant	Concentration (mol L-1)	Flow rate (µL/h)
Au	0.025	80
4-ATP	10^{-2}	20
	10^{-4}	
	10^{-6}	
	10^{-8}	

After that, the microfluidic device was disconnected from the syringe pump (300-New Era Pump System) and placed on the Raman spectrometer

(DXR Thermo Scientific) to set the analysis parameters showed in table 5 and to run the measurement.

Table 5. SERS measurement parameters.

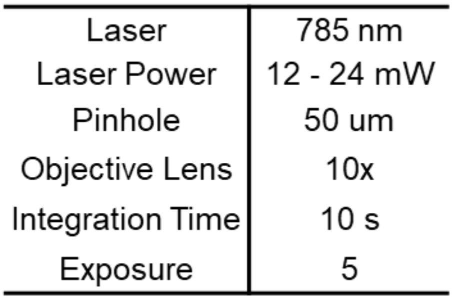

Laser	785 nm
Laser Power	12 - 24 mW
Pinhole	50 um
Objective Lens	10x
Integration Time	10 s
Exposure	5

CHAPTER IV

RESULTS AND DISCUSSION

4.1. Design and Microfabrication of Microfluidic Devices.

4.1.1. Design and Microfabrication of PDMS/glass Microfluidic Devices

Figure 10 shows the 4 inches Ø Si wafer framework provided by Group 7 at ICMCB. This framework has alignment marks as a reference cut points for its proper handling during and after microfabrication.

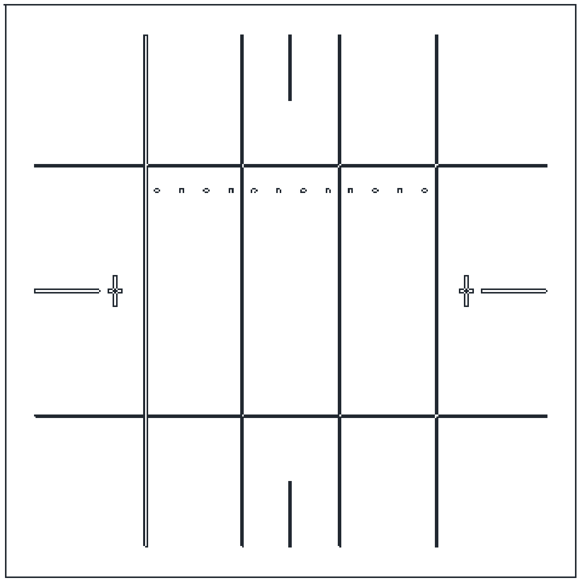

Figure 10. 4 inches Ø Si wafer framework for a 55 mm in width and 64 mm in length microfluidic device.

Figure 11 shows the first microfluidic design, where three microfluidic devices were drawn. Besides, the size reduction of the devices permits the microfabrication of more than one chips and avoid the excessive use of more wafers or reactants.

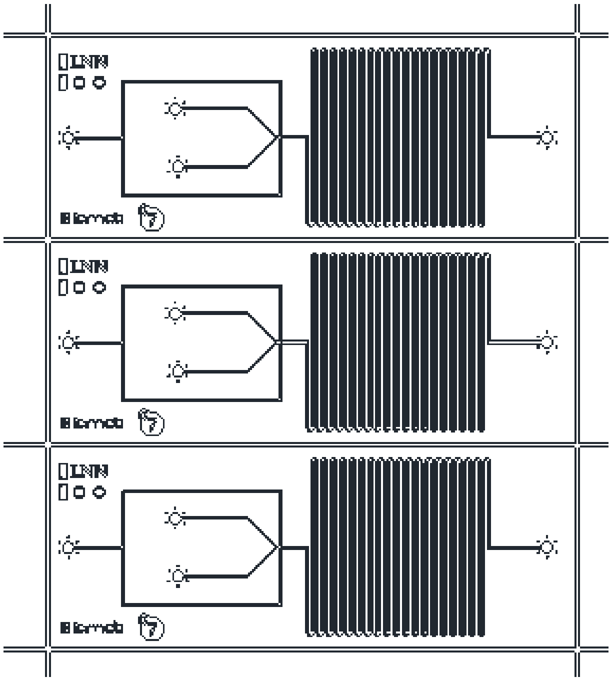

Figure 11. First mask design with three microfluidic devices.

In Figure 12, it is observed a larger microfluidic device design. This larger design allows a better manipulation of the chip. On the other hand, by presenting a larger mixer, the increment of residence times would perform the chemical reactions that occur within it[92].

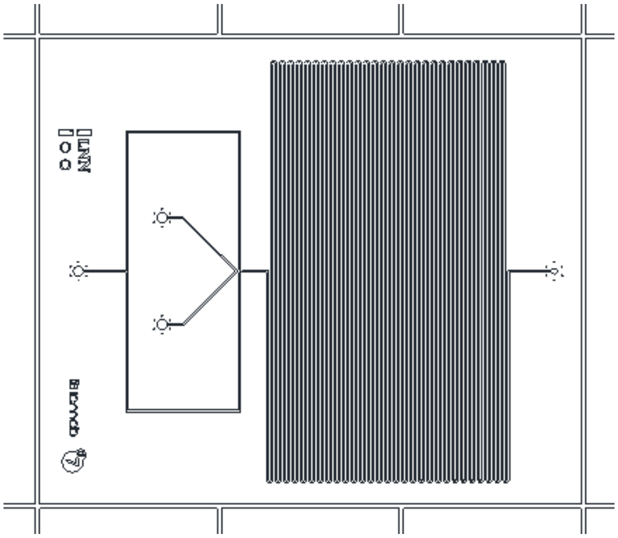

Figure 12. Second mask design with a larger microfluidic device.

Also, these design presents a serpentine rounded-corner mixer due to some studies report that with this geometry could improve the mixing efficiency and prevent the damage in the samples. Also, the rounded corners improve the efficiency of the light transmission inside the devices, favoring some noble metal synthesis[93].

After the microfabrication, two master molds were obtained. We measured the width and height of microchannels with a profilometer. Figure 13 shows the first design and the height profiles of each chip.

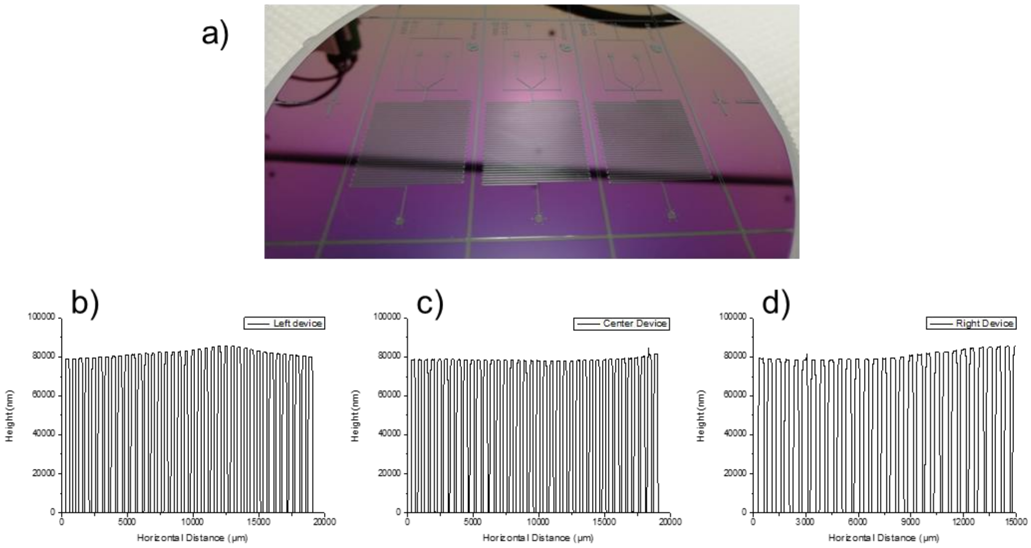

Figure 13. a) First master mold. b) Left chip height profile. c) center chip height profile. d) Right chip height profile.

As we can see, exist a low difference between each device in their height due to the expansion of the photoresist resin from the center to the borders because the spin-coating rotation (Fig 13b-d). This variation was minimum that we could despise it. In average, the height of the microchannels was 85 µm.

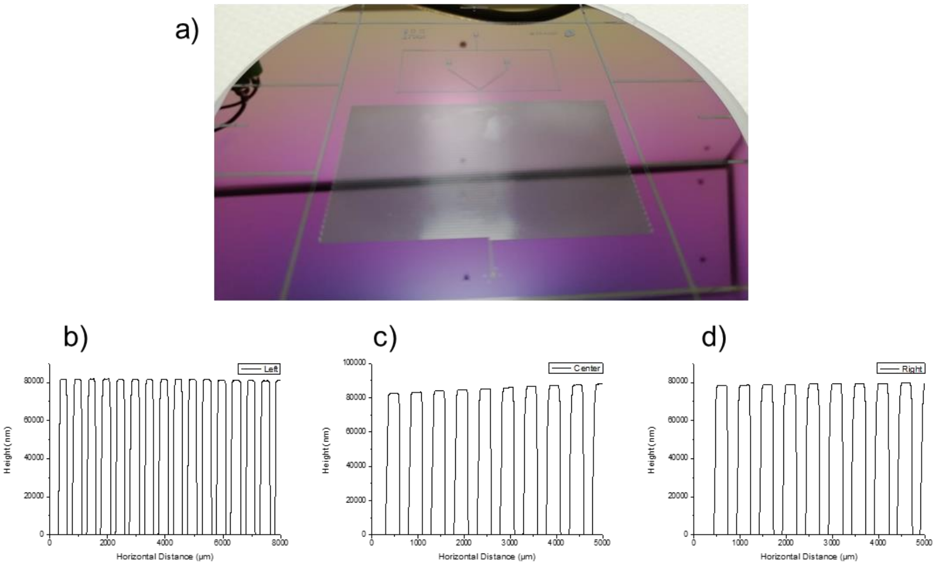

Figure 14. a) Second master mold. b) Left zone profile. c) center zone profile. d) Right zone height profile.

Figure 14 shows the second design with its height profile. This master mold was measured in three different mixer zone for try to obtain a representative average of microfluidic microchannels heights, surrounding on 85 µm. We could observe a slightly variation on the heights due to same tendency explained above.

To calculate the residence time of each synthesis inside each reactor, the reactor volume was calculated multiplying the mixer area from the bottleneck just in the junction of reactants microchannels to just before the outlet by the correspondent heights, obtaining 12.3 mm^3 and 48.5 mm^3 (12.3 µm and 48.5 µm) for first and second design, respectively.

Then, following the procedure, three PDMS/glass devices were obtained. The dimensions of each devices were 26 mm of width, 76 mm of length and 5 mm of height. Figure 15 shows the complete setup that was employed in each experiment using the PDMS/glass devices. I.D. 80 µm PEEK tubes were used for flow all the reactants, following the droplet generation with an optical microscope.

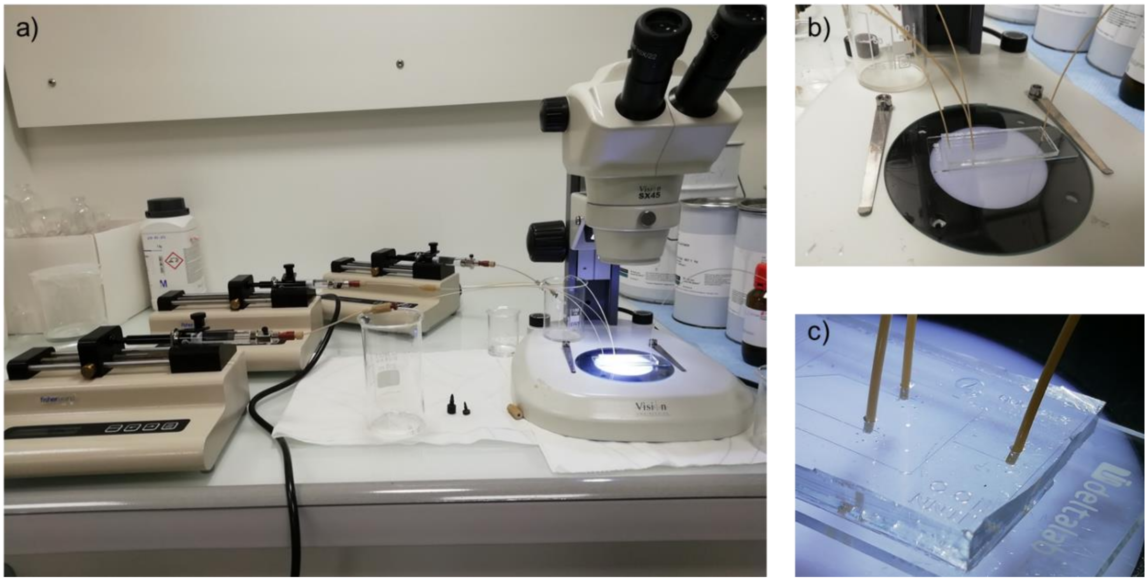

Figure 15. a) PDMS/glass device setup. b) PDMS/Glass device. c) Image magnification of PDMS/Glass inlets.

4.1.3. Design and Fabrication of Microfluidic Tubing Reactor

After following the procedure mentioned in 3.1.3 section, the microfluidic synthesis setups for Ag and Au obtained were the showed in Figure 16.

Figure 16. a) Microfluidic tubing reactor for Ag nanoparticles synthesis. b) Microfluidic tubing reactor for Au nanoparticle synthesis.

For Ag synthesis, a tubing with 0.46 mL volume was plugged. Au synthesis employed a 0.87 mL volume tubing and was coiled and submerged in an oil bath to start the reaction heating it.

4.2. Microfluidic Synthesis of Noble Metal Nanoparticles

4.2.1. Ag nanoparticles synthesis with PDMS/glass microfluidic device

Table 6 shows all conditions employed for each Ag NPs microfluidic synthesis.

Table 6. Flow rate conditions for microfluidic Ag nanospheres synthesis using PDMS/glass microfluidic devices.

Sample	PDMS-Ag1	PDMS-Ag2	PDMS-Ag3
Reagents	Flow rate (mL/h)		
Ag^+	0.10	0.15	0.05
BH_4^-	0.10	0.05	0.15
Silicone Oil 0.3% wt. Span 80	0.35		
Qt	0.55 mL/		

In all experiments, the droplet generation was controlled, favoring the dripping regime at these total flow rates. Likewise, the droplet coalescence problem was avoided thanks to the addition of the surfactant, eliminating the electrostatic forces on the surface droplets, which is strong at this volume levels

(Appendix A)[94]. However, we can see two problems in Figure 17a, an Ag nucleation in the reactant microchannels intersection and, in Figure 17c, a clogging effect through the serpentine mixer.

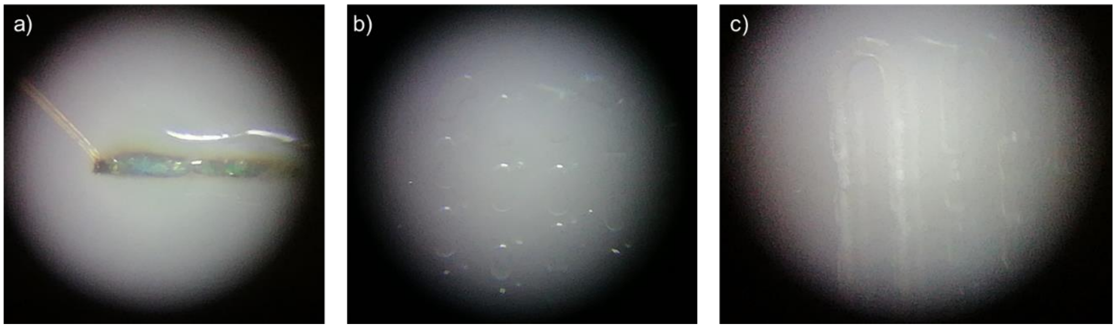

Figure 17. Micrographs of Experiment 1. a) Ag growth through reactants microchannel intersection. b) Droplets flow through the serpentine mixer. c) Clogging effect through the serpentine mixer.

To understand the first problem, it is necessary to know if the flow regime presents in this zone is a laminar flow.. For demonstrate this, the Reynolds number must be below 2000 and could be calculated using the equation 28, considering equal wettability properties on all microchannel walls[95]. On the other hand, if we considering $U = \frac{Q}{A}$, and $v = \frac{\rho}{\mu}$ we obtain the equation 34.

$$Re = \frac{QD_H}{vA} \tag{34}$$

Where, Q, A and v are the total flow rate, cross-section area and viscosity of the fluid, respectively. To resolve this, the value of each variable is showed in Table 7.

Table 7. Variable values for Reynolds number calculation.

Q	$5.555\text{x}10^{-12}$ m^3/s
D_H	$1.2\text{x}10^{-4}$ m
v	$1\text{x}10^{-4}$ m^2/s
A	$1.7\text{x}10^{-8}$ m^2

Although, we could consider the viscosity change in each aqueous syringe due to the ions dissolve, however, could be despised and consider the pure water viscosity at 25 °C. Also, the flow rate, Q, was the sum of each water syringe flow rate. Hydraulic diameter, D_H, was considered for rectangular cross-section microchannels. Equation 32 explains this.

$$D_H = \frac{4A}{P_{wet}} \tag{32}$$

Where, A is the cross-section area and P_{wet} is the wet perimeter of the microchannels walls.

Resolving the Reynolds number equation with this data, we obtain a value of 3.9×10^{-3}, being the viscosity forces the ones that govern the flow of the fluid and describes the fluid flow as laminar flow. With this on mind and considering that fluid as a continuum through all the channel as well as a Newtonian fluid, we can refer to the famous Navier-Stokes equation that describes the velocity field of an incompressible fluid in an empirical way[96].

$$\rho \frac{\partial u}{\partial t} + \rho u \cdot \nabla u = -\nabla p + \eta \nabla^2 u + f \qquad (33)$$

$$\nabla \cdot u = 0$$

In the equation 33, the left term describes the time-space velocity field dependency, regarding on the inertial forces as fluid density. On the other hand, the right term considers the viscosity coefficient as a shear stress between the fluid and its environment during its flow, the driving forces as pressure field and the external forces as gravity or electrostatic forces.

On the other hand, on microfluidic systems, the equation could be simplified due to, typically, the flow regime is laminar flow, and it is possible to considerate a 2D flow system. Now, in our system, we demonstrated that the flow regime is laminar, domaining the viscous forces on the fluid flow. This fluid flow field can be described with the “solved” Stoke equation if we considered the no-slip boundary condition[97].

$$-\nabla p + \eta \nabla^2 u = 0 \tag{34}$$

This boundary condition supposes a state that the velocities at phase boundaries as wall-liquid or liquid-liquid, must be equal. This means that for flow of a liquid inside of a microchannel, the fluid velocity at the wall must be zero.

With this, we can describe the fluid flow with streamline of fluid like layers. Figure 18 shows the fluid flow field proposed on Ag growth zone.

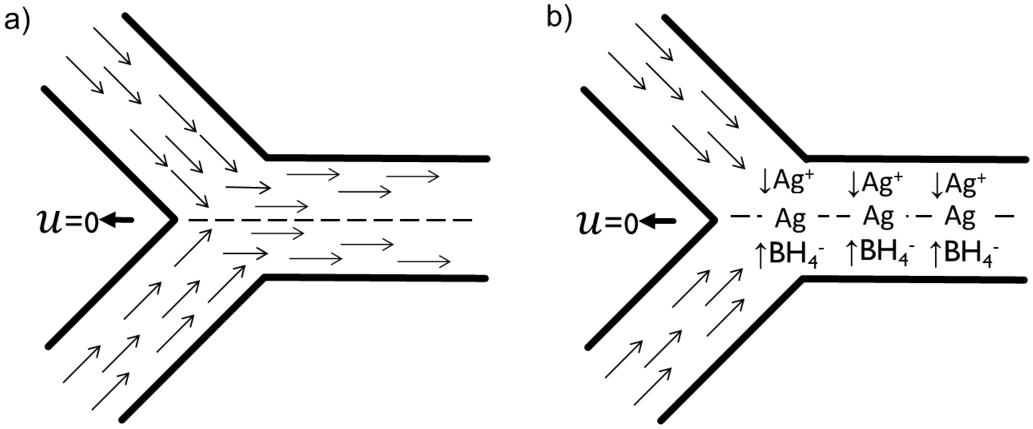

Figure 18. Fluid flow field of Ag nanosphere synthesis using PDMS/Glass device.

Besides, at this flow regime, the diffusion and convection transport phenomena are higher than macroscale systems due to at microscale, the matter quantity is “packed” in small volumes, doing the mass transport fast, favoring kinetically the reaction[98]. In addition to this, the higher reduction potential of $NaBH_4$ favors thermodynamically the Ag synthesis. We could say that this Ag growths occurs spontaneously.

The second problem regarding the sample PDMS-Ag1, is the clogging effect, appearing after few minutes. This effect commits to the homogeneity of the reaction and monodispersity of the nanoparticles[99].

Although the application of the mixer is to increase the mixing within the droplets and favor the chemical reaction, it also did so by generating a highly stable emulsion between the oil and the aqueous phase. This because of, in general, the velocity of the fluids is not continuous due to inertia product to non-homogenous surface properties in the microfluidic device[100]. This same behavior is presented in the experiment 2 and 3.

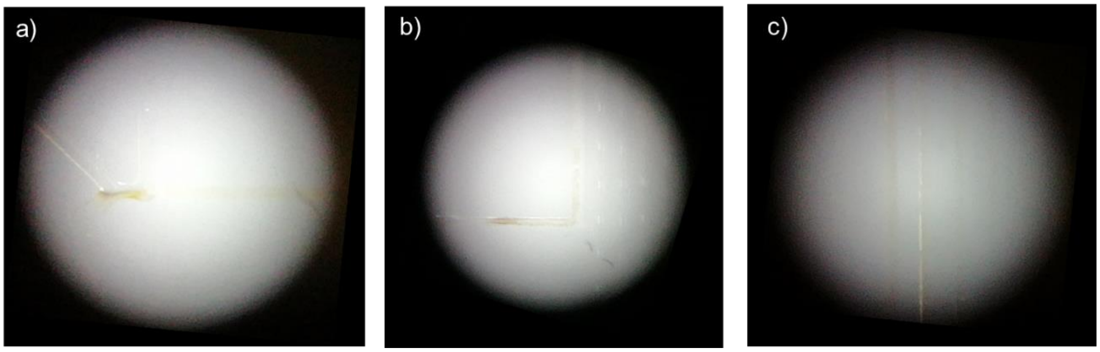

Figure 19. Micrographs of Experiment 2 and 3. a) Ag growth through reactants microchannel intersection of the experiment 2. b) Ag growth after droplet generation of the experiment 3. c) Clogging effect and Ag growth through the serpentine mixer.

On the other hand, in Figure 19, experiment 2 and 3 shows an Ag growth on the mixer. This effect could be explained with this surface properties problem explained before due to after velocity stabilization in segmented-flow microfluidic devices, droplets must be surrounded by the continuous phase and flow at a constant velocity. However, the aqueous phase is dragged due to the hydrophilic property of the glass, producing the condition explained above (Figure 20)[101].

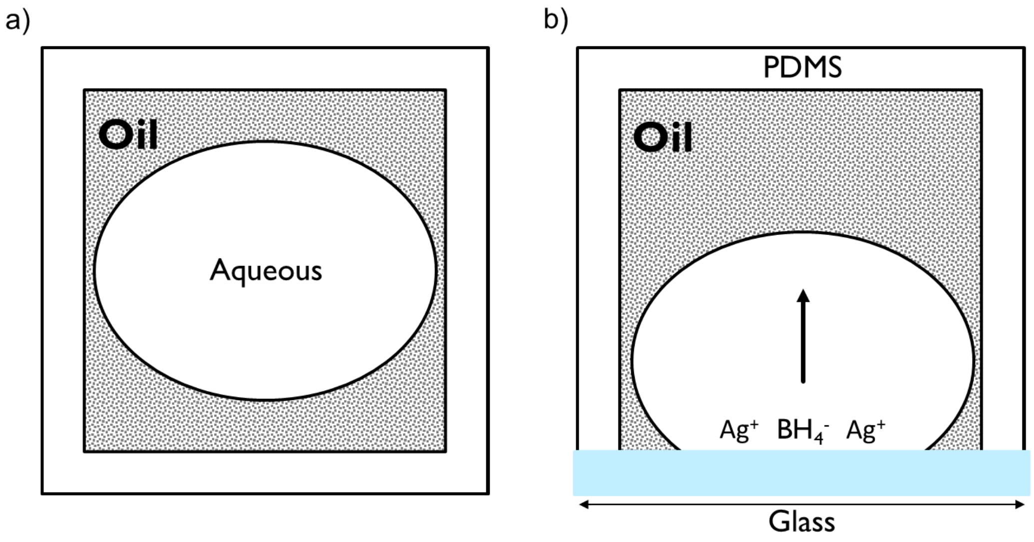

Figure 20. a) ideal fluid flow through a microchannel in a segmented-flow microfluidic device. B) Real flow in our PDMS/Glass microfluidic devices.

With all these problems, the noble metal nanoparticle synthesis using PDMS/glass devices was not continued, preferring microreactors with homogenous surface properties as tubing reactor.

4.2.2. Ag nanoparticles synthesis with Microfluidic tubing reactor.

Figure 21 shows the Ag-1 and Ag-2 UV-Vis spectra, respectively. The Ag-1 absorption spectrum exhibits the classical LSPR signal for spherical-shaped Ag NPs at λ_{max} = 400 nm[102]. This LSPR signal is related with the coherent collective oscillation of the valence electrons in the metal NPs and it depends on their size and shape[103]. On the other hand, sample Ag-2 shows two LSPR signals. One l at λ_{max} = 418 nm and other at λ_{max} = 569 nm, which could be attributed to the formation of Ag NPs with sizes from 45 to 100 nm. Besides, the Ag-1 maximum absorption is more than 50 times greater than Ag-2, attributed to the higher conversion yield for the Ag-1 conditions.

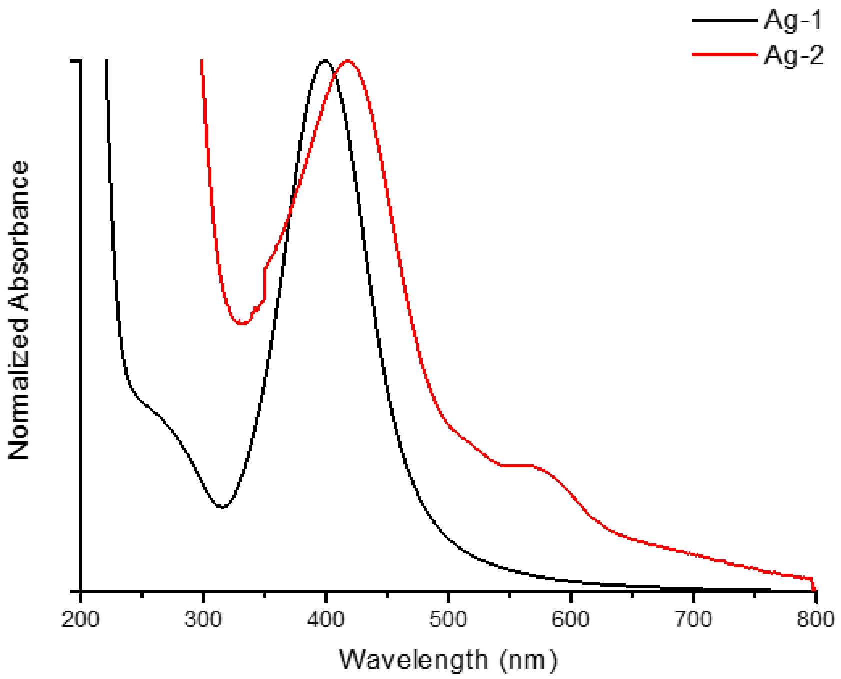

Figure 21. Normalized UV-Vis spectra of Ag NPs suspensions for samples Ag-1 (1x) and Ag-2 (56x).

Figure 22a shows the Ag NPs obtained at 0.6 min of RT (Ag-1), observing spherical morphologies of 4.2 ± 1.4 nm of size, being a typical size for these kind of morphologies with LSPR like the UV-Vis spectrum observed[102]. Nevertheless, it can also be seen larger particles (Figure 22b), generating polydispersity. This effect could be due to potential interactions between the

Na_3Cit and the silicon oil continuous phase. Na_3Cit can act as a surfactant, could stabilize some silicon oil inside the aqueous phase, modifying the chemical reaction and thereby the Ag NPs growth[104]. Additionally, the used of $NaBH_4$ as a reducing reagent generate hydrogen, which cannot be extracted from the liquid-liquid segmented flow. This generated hydrogen might also affect the chemical reaction, and consequently the nanoparticles growth mechanisms[105]. The use of a three-phase flow (liquid/liquid /gas) could therefore be considered to solve this problem, as reported in the literature[106].

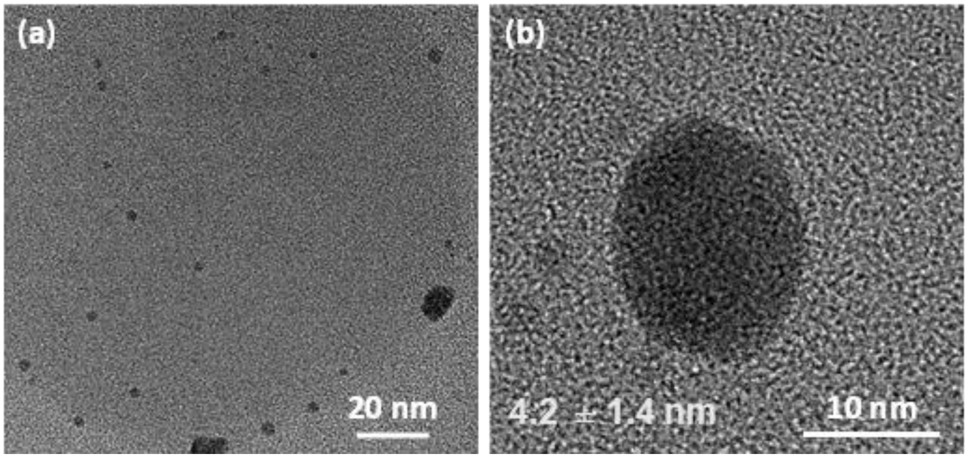

Figure 22. TEM images of Ag nanoparticles obtained at 0.6 min of RT. a) Ag nanoparticles surrounding an oil droplet. b) Ag nanoparticle

Sample Ag-2 did not produce enough amount of Ag nanoparticles to be characterized helped by TEM. However, based on the UV-Vis absorption spectrum, can be mentioned that larger polydispersity is present, due to the flow conditions at larger RT. By increasing the RT (and therefore reducing flow rates), the shear stress decreases, hindering the fluid deformation and, consequently the mixing process inside the droplets[107]. The mixing is critical in this fast reduction reaction since multiple nucleation steps can occur if the reagents are not quickly mixed, resulting in large particles size distribution.

4.2.3. Au nanoparticles synthesis with Microfluidic tubing reactor

Gold nanoparticles were synthesized at different flowrates, maintaining all the other parameters constant such as the temperature of the oil bath (105 °C) and the $HAuCl_4$:Na_3Cit flowrates ratio at 1:1 (resulting in a concentration ratio of 1:138). Figure 23 shows the Au-1, -2, -3 and -4 absorption spectra.

Two effects can be observed. First, higher RT results in an absorbance intensity increase, which can be directly related to a higher concentration of Au NPs. Second, we can observe a blue shift coupled to a narrowing of the LSPR with an increasing residence time. This could n be explained by a narrowing of the particle size distribution at longer residence times, resulting in an Au NPs optical properties improvement. This could be related to the RT of the fluid due to at lower RT, the fluid is not heated as faster as the chemical reaction needs, disadvantaging the Au nanoparticle obtention. On the other hand, at higher RT, the fluid is heated enough to start the reduction of $AuCl_4^-$ to Au^0 and stabilize the nanoparticles, improving the Au nanoparticle production[108].

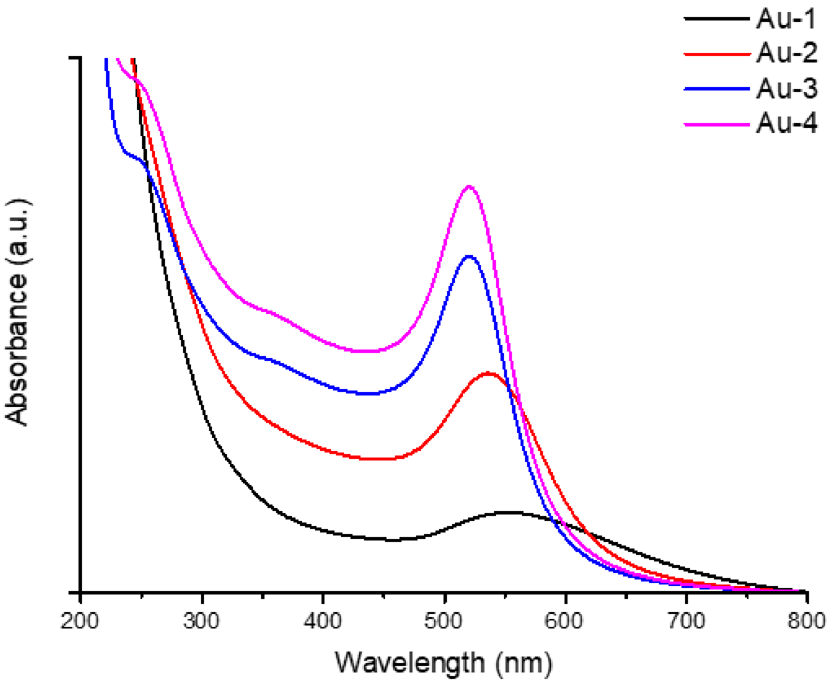

Figure 23. UV-Vis spectra of Au NPs suspension obtained for samples Au-1, Au-2, Au-3, Au-4.

Considering the short residence times (samples Au-1 and Au-2), compared to this, sample Au-1 presents the lowest absorbance and a red shifted LSPR at 550 nm. This could be related to low reaction control due to mixing and heating problems previously explained as well as bigger nanoparticle sizes, scattering lighter because of a larger optical cross-section[109]; non-spherical morphologies[110] and nanoparticle aggregations[111] (Figure 24a and c). However, due to a higher RT than Au-1, the sample Au-2 presents a LSPR at 540 nm, nanoparticles with spherical morphologies and non-aggregation problems, as is observed in Figure 24e and g. Also, in all TEM images, is possible to observe impurities regarding to oil droplet traces, hindering to zoom in the sample.

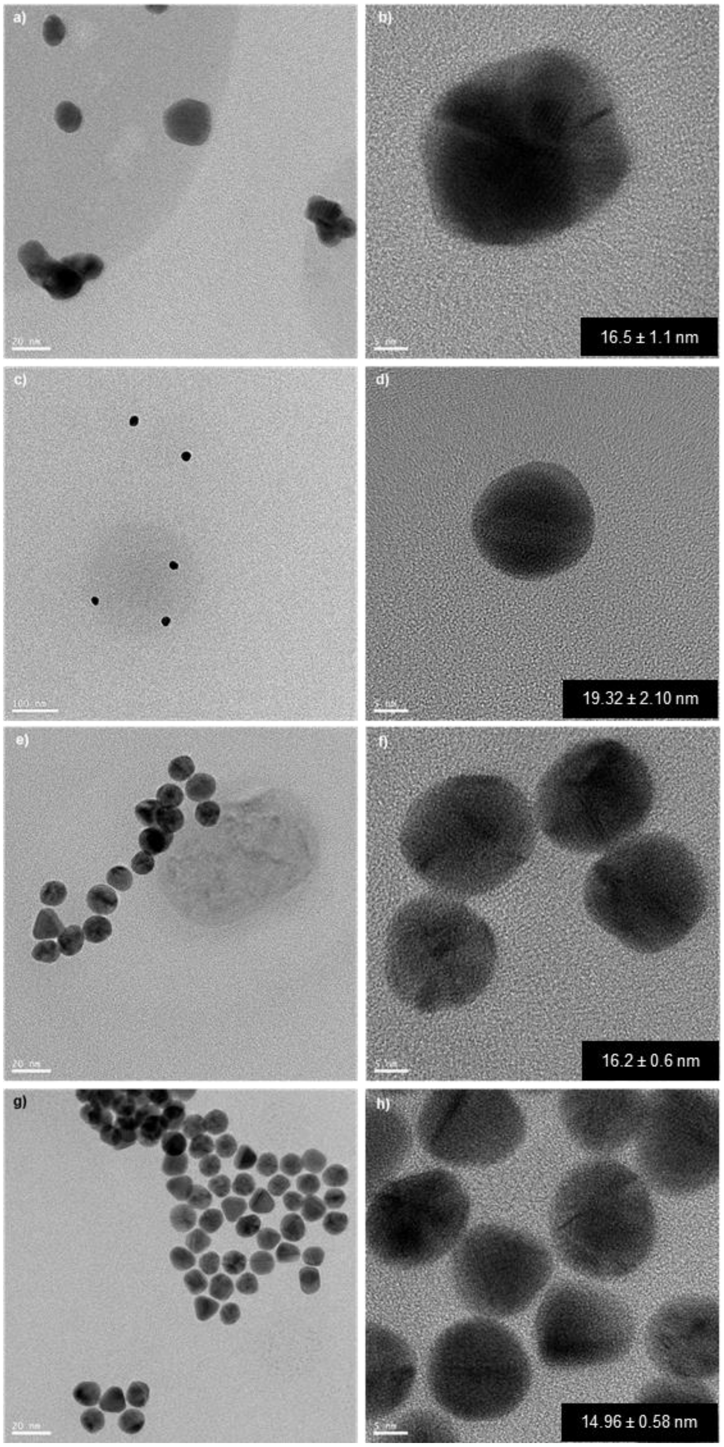

Figure 24. TEM images of (a-b) Au-1, (c-d) Au-2, (e-f) Au-3 and (g-h) Au-4.

Oppositely, for the longer residence times, the characteristic LSPR of Au spherical-shaped nanoparticles at 520 nm in the samples Au-3 and Au-4, indicating nanoparticle sizes around 15-18 nm[111]. This is confirmed by the TEM measurements (Figure 24e-h) showing spherical Au NPs with average sizes of 16.23 ± 0.63 and 14.96 ± 0.58 nm, respectively. However, other morphologies are presented. This could be regarding to the presence of light in the synthesis[112], even if the reactor were covered. On the other hand, the Figure 25a indicates the characteristic crystal planes [111], [200],[220] and [311] for metallic gold. Also, Figure 25b shows that the samples obtained are polycrystalline.

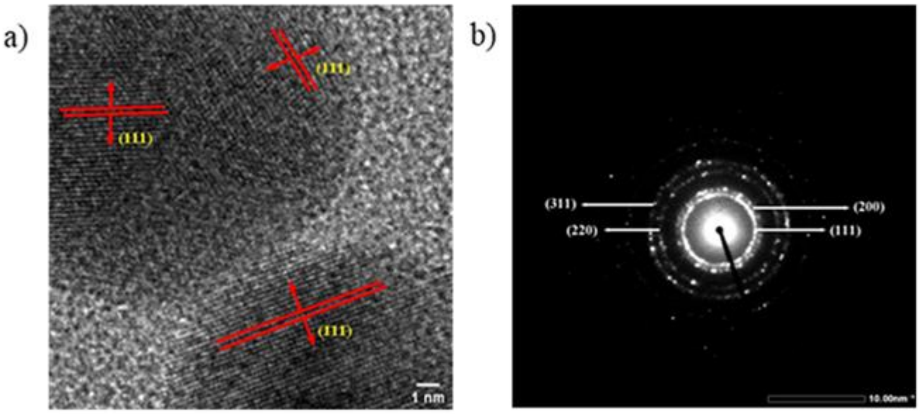

Figure 25. a) HR-TEM image of sample Au-2 and b) Selected Area Electron Diffraction (SAED).

Additionally, Figure 22 is shown an absorbance band narrowing when the RT increase, speaking about an improvement in the monodispersity of the nanoparticles[113].

4.3. Microfluidics and Surface Enhanced Raman Spectroscopy

4.3.1. Design and Microfabrication of Si/Pyrex Microfluidic Devices

Figure 26 shows the three different designs (0.2 mm width and 0.1 mm depth) of Si/Pyrex microfluidic devices that were fabricated. The first design (Fig. 26a) presents two inlets and one outlet of 1.2 mm Ø each, intersecting at 45° in a single microchannel, with co-flow geometry to avoid what is observed in flow-focusing systems obtained from PDMS/Glass devices[114]. The other two design (Fig. 26b and c) have only one inlet and outlet of 1.2 mm Ø and 6.34 cm length, allowing to reduce the fabrication cost. On the other hand, each serpentine design was drawn to improve the mixing processes where each microchannel loop distances were 3.8 mm to consider the Raman objective lens size to perform the SERS measurement at only in one microchannel.

After fabricating them, we functionalized all the microfluidic devices, following the flow conditions previously describe.

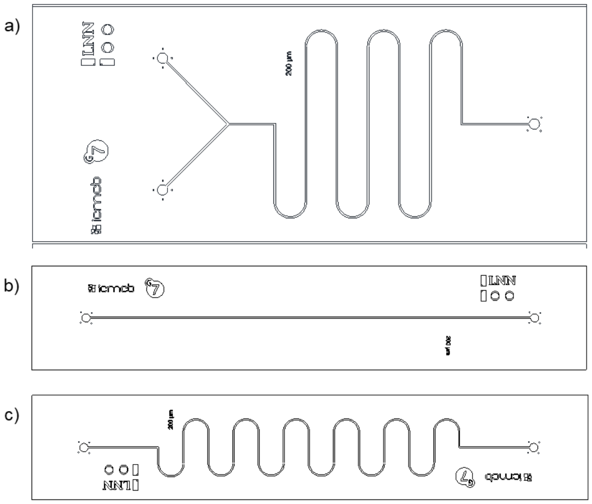

Figure 26. New microfluidic device designs for noble metal nanoparticle assembly strategy. a) Two inlets device design, b) one straight inlet design and c) one serpentine inlet design.

4.3.2. Microfluidic-SERS Analysis

After carrying out the silanization process in each microfluidic devices, every 4-ATP concentration shown above in table 3 was flowed through the microchannels, measuring each sample in the Raman spectrometer as blanks.

Fig. 27 shows the respective Raman spectra. It should be noted that the most dilute sample was not included, since neither Raman nor SERS signal was detected. It is important to highlight that only the designs shown in Fig 26b and c were used to perform the SERS analyses due to equipment space.

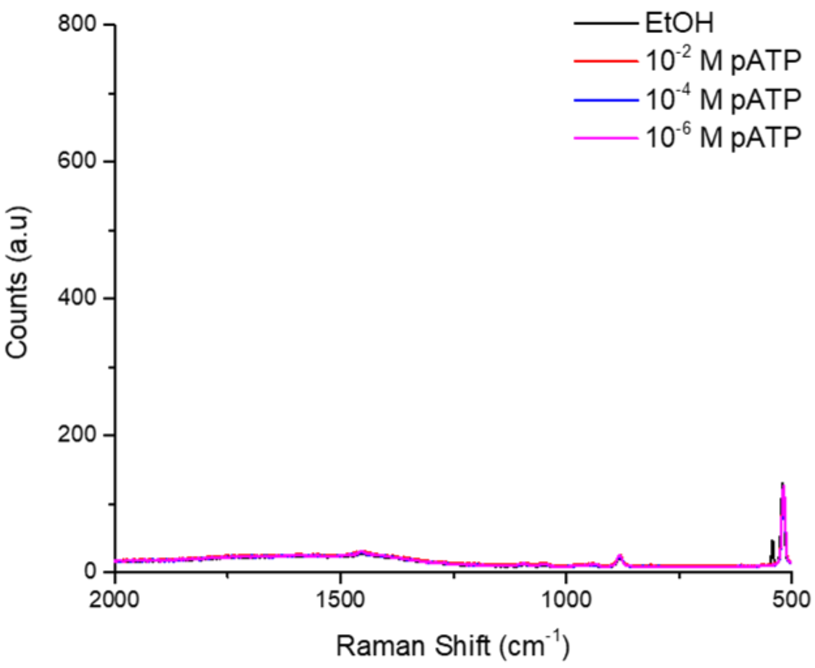

Figure 27. Raman spectra of 4-ATP blanks.

Once blanks were measured, the microfluidic SERS substrates were prepared following Table 4 conditions and, to select the laser power, 4-ATP sample at 10^{-2} mol L^{-1} was chosen.

Fig. 28 shows the Raman spectrum at 12 (red line) and 24 mW (black line), realizing the characteristic vibration signals of the 4-ATP molecule at 1590 and 1080 cm-1, corresponding respectively to bending S-C and benzene ring C-C bonds[115, 116]. Also, we can observe that it is measures without any surface functionalization, the molecule probe is not even detected, observing a SERS effect when the Au nanoparticles are present due to their microfluidic assemble thanks to 3-MPTMS.

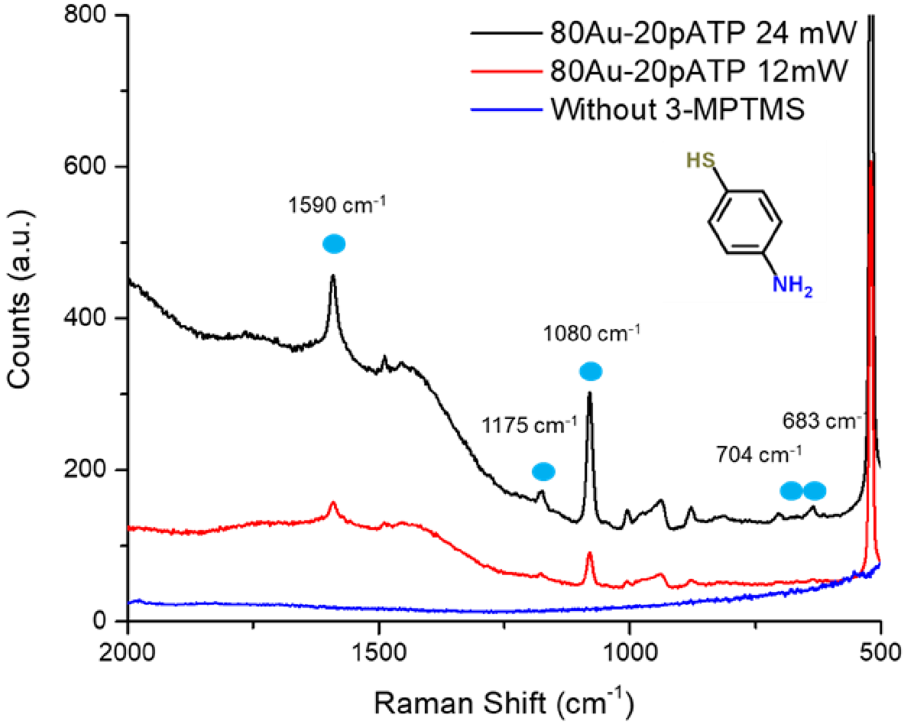

Figure 28. SERS spectra of 4-ATP 10-2 mol L-1 at 12 (red line) and 24 mW (black line) of laser power.

On the other hand, an Analytical Enhance Factor (AEF) was calculated following the equation 35, where I_{SERS} and I_{Raman} are the signal intensity of SERS and Raman measurement, respectively; and C_{SERS} and C_{Raman} are the analytical concentration of the molecule probe used in SERS and Raman analysis.

$$AEF = \frac{I_{SERS} \times c_{SERS}}{I_{Raman} \times c_{Raman}} \tag{35}$$

The 4-ATP Raman signals were increased 17 times more than the blank, observing that there is indeed a SERS effect when the Au nanoparticles are flowed after silanization process, increasing the Raman intensity.

This is because when the Si surface is activated with hydroxyl groups (Figure 29a), the 3-MTPMS is condensate (Figure 29b), forming an irreversible Si-O-Si bonding (Figure 29c). Then, Au nanoparticles are caught by mercapto groups, which due to their gold lability, ensure the detection of 4-ATP by SERS.

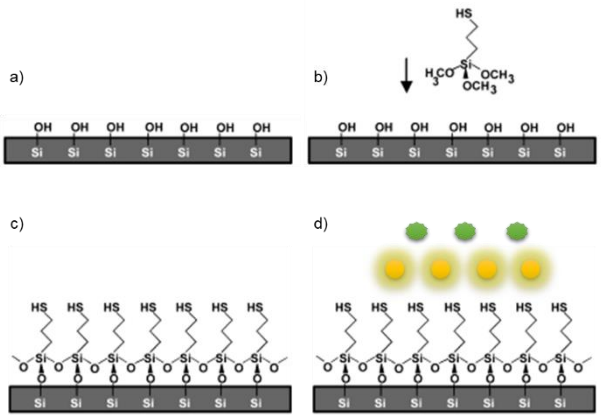

Figure 29. Microfluidic assembly strategy. a) hydroxy surface activation. b) 3-MTPMS flow through the microchannel. c) Si surface functionalization with 3-MTPMS. d) Noble metal nanoparticle catching (yellow dot) and molecule probe charge to analysis (green dot).

Due to the Raman signal increment, it was decided to continue at 24 mW of laser power for samples 10^{-4} and 10^{-6} mol L^{-1} to favor their detection.

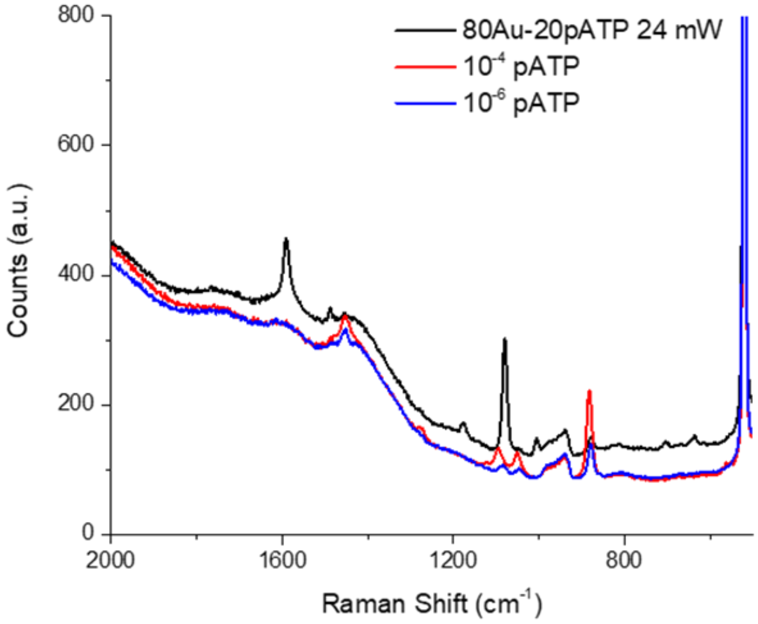

Figure 30. SERS spectra of 10-2, 10-4 and 10-6 mol L-1 of 4-ATP at 24 mW of power laser.

After what was demonstrated in the previous experiment, the following sample concentrations (10^{-4} and 10^{-6} mol L^{-1}) were carried out at 24 mW, observing in Fig. 30 that the detection of the characteristic signals of 4-ATP is null. Although it may be due to this dilution effect, it should be considered that the incident laser must pass through the glass material to the bottom of the microchannel and return along the same path, losing energy or overlapping the signals of the sample with the microfluidic device signals.

It is important to highlight that the objective lens used was a short-range one, and it is recommended to carry out this type of analysis work with a long-range objective lens to reduce this effect.

CHAPTER V

CONCLUSIONS

Two different microfluidic reactors were designed and fabricated to synthesize noble metal nanoparticles. The soft lithography method permitted to fabricate reproducible PDMS/glass microfluidic devices. However, after several observations, it is concluded that the surface properties combination between PDMS and glass do not allow the noble metal nanoparticle synthesis in a reproducible way.

On the contrary, microfluidic tubing reactor permitted the synthesis so much Ag as Au NPs due to homogenous surface properties. Thanks to Ag microfluidic synthesis results obtained, it is possible to conclude that, 0.6 min of RT produces nanoparticles of 7 nm with spherical-shaped morphology, characteristic to LSPR at 400 nm. However, 3 min of RT did not produce Ag nanoparticles.

For Au nanoparticle synthesis, 3 min of RT generates polydisperse, agglomerated and red-shifted Au nanoparticles at 550 nm. On the other hand, 5, 10 and 20 min of RT produce Au spherical-shaped nanoparticles. This last two conditions generate Au nanoparticles of 16.5 and 17 nm, respectively with a typical observed LSPR at 520 nm. This demonstrate that increasing RT improves the production of these nanoparticles and their monodispersity as well as the possibility to synthesize noble metal nanoparticles using microfluidics.

On the other hand, photolithography allowed obtaining Si/glass microfluidic devices as SERS substrates. The functionalization of the microchannels with 3-MPTS allowed the assembly of Au nanoparticles, increasing the typical vibrational signals of 4-ATP (1590 and 1080 cm-1) due to the SERS effect present. However, the entire system only allowed the detection of this molecule at a concentration of 10-2 mol L-1, having an AEF of 17.

REFERENCES

1. F. Capital, L. Contra, and E. L. Narco, “México, país de tránsito y elaboración de drogas,” El Economista, 2018. [Online]. Available: https://www.eleconomista.com.mx/politica/Mexico-pais-de-transito-y elaboracion-de-drogas-20170302-0040.html. [Accessed: 24-Jul-2019.

2. B. We, “Operation Fast and Furious Fast Facts,” CNN, 2019. [Online]. Available: https://edition.cnn.com/2013/08/27/world/americas/operation-fast-and-furious-fast-facts/index.html. [Accessed: 24-Jul-2019].

3. World Health Organization, “Key facts about cancer,” World Health Organization, 2018. [Online]. Available: https://www.who.int/cancer/about/facts/en/. [Accessed: 24-Jul-2019].

4. World Health. Organization, “Tuberculosis,” World Health Organization. [Online]. Available: https://www.who.int/news-room/fact-sheets/detail/tuberculosis. [Accessed: 24-Jul-2019].

5. WHO. (2018). Pesticide residues in food. https://doi.org/10.1046/j.1525-1594.2002.06876.x.

6. Stuart, B. (2000). Infrared spectroscopy. Kirk-Othmer Encyclopedia of Chemical Technology, 1-18.

7. Chalmers, J., & Griffiths, P. (2002). Handbook of Vibrational Spectroscopy, 5 volumes set. Wiley.

8. Siesler, H. W. (2016) Vibrational Spectroscopy. Elsevier.

9. Skoog, D. A., Holler, F. J., & Crouch, S. R. (2017). Principles of instrumental analysis. Cengage learning.

10. B. H. Stuart, Infrared Spectroscopy: Fundamentals and Applications. 2005.

11. Smith, B. C. (2011). Fundamentals of Fourier transform infrared spectroscopy. CRC press.

12. Rouessac, F., & Rouessac, A. (2013). Chemical analysis: modern instrumentation methods and techniques. John Wiley & Sons.

13. The Nobel Prize in Physics 1930. NobelPrize.org. Nobel Media AB 2019. Wed. 4 Sep 2019. https://www.nobelprize.org/prizes/physics/1930/summary/.

14. Raman, C. V., & Krishnan, K. S. (1928). Polarisation of scattered light-quanta. Nature, 122(3066), 169.

15. Colthup, N. (2012). Introduction to infrared and Raman spectroscopy. Elsevier.

16. Armenta, S., Quintas, G., Garrigues, S., & De la Guardia, M. (2005). Mid-infrared and Raman spectrometry for quality control of pesticide formulations. TrAC Trends in Analytical Chemistry, 24(8), 772-781.

17. Geiman, I., Leona, M., & Lombardi, J. R. (2009). Application of Raman spectroscopy and surface-enhanced Raman scattering to the analysis of synthetic dyes found in ballpoint pen inks. Journal of forensic sciences, 54(4), 947-952.

18. Cao, Y. C., Jin, R., & Mirkin, C. A. (2002). Nanoparticles with Raman spectroscopic fingerprints for DNA and RNA detection. Science, 297(5586), 1536-1540.

19. Zachhuber, B., Ramer, G., Hobro, A., & Lendl, B. (2011). Stand-off Raman spectroscopy: a powerful technique for qualitative and quantitative analysis of inorganic and organic compounds including explosives. Analytical and bioanalytical chemistry, 400(8), 2439-2447.

20. Fleischmann, M., Hendra, P. J., & McQuillan, A. J. (1974). Raman spectra of pyridine adsorbed at a silver electrode. Chemical physics letters, 26(2), 163-166.

21. King, F. W., Van Duyne, R. P., & Schatz, G. C. (1978). Theory of Raman scattering by molecules adsorbed on electrode surfaces. The Journal of Chemical Physics, 69(10), 4472-4481.

22. Hartstein, A., Kirtley, J. R., & Tsang, J. C. (1980). Enhancement of the infrared absorption from molecular monolayers with thin metal overlayers. Physical Review Letters, 45(3), 201.

23. Hatta, A., Ohshima, T., & Suetaka, W. (1982). Observation of the enhanced infrared absorption of p-nitrobenzoate on Ag island films with an ATR technique. Applied Physics A, 29(2), 71-75.

24. Guillot, N., & de la Chapelle, M. L. (2012). The electromagnetic effect in surface enhanced Raman scattering: Enhancement optimization using precisely controlled nanostructures. Journal of Quantitative Spectroscopy and Radiative Transfer, 113(18), 2321-2333.

25. Hu, Y. (2019). Surface-Enhanced Infrared Attenuated Total Reflection Spectroscopy based on Carbon Nanomaterials (Doctoral dissertation, Universität Ulm).

26. Yang, X., Sun, Z., Low, T., Hu, H., Guo, X., Garcia de Abajo, F. J., ... & Dai, Q. (2018). Nanomaterial-Based Plasmon-Enhanced Infrared Spectroscopy. Advanced Materials, 30(20), 1704896.

27. Betz, J. F., Yu, W. W., Cheng, Y., White, I. M., & Rubloff, G. W. (2014). Simple SERS substrates: Powerful, portable, and full of potential. Physical Chemistry Chemical Physics, 16(6), 2224–2239. https://doi.org/10.1039/c3cp53560f.

28. Li, W., Zhao, X., Yi, Z., Glushenkov, A. M., & Kong, L. (2017). Analytica Chimica Acta Plasmonic substrates for surface enhanced Raman scattering. Analytica Chimica Acta, 984, 19–41. https://doi.org/10.1016/j.aca.2017.06.002.

29. Fan, M., Andrade, G. F., & Brolo, A. G. (2011). A review on the fabrication of substrates for surface enhanced Raman spectroscopy and their applications in analytical chemistry. Analytica chimica acta, 693(1-2), 7-25.

30. Le Ru, E. C., & Etchegoin, P. G. (2012). Single-molecule surface-enhanced Raman spectroscopy. Annual review of physical chemistry, 63, 65-87.

31. Thiele, M., Götz, I., Trautmann, S., Müller, R., Csáki, A., Henkel, T., & Fritzsche, W. (2015). Wet-chemical passivation of anisotropic plasmonic nanoparticles for LSPR-sensing by a silica shell. Materials Today: Proceedings, 2(1), 33-40.

32. Castillo-León, J., & Svendsen, W. E. (Eds.). (2014). Lab-on-a-Chip devices and micro-total analysis systems: a practical guide. Springer.

33. Whitesides, G. M. (2006). The origins and the future of microfluidics. Nature, 442(7101), 368.

34. Kang, K., Lee, B., & Lee, C. (2019). Recent progress in the synthesis of inorganic particulate materials using microfluidics. Journal of the Taiwan Institute of Chemical Engineers, 98, 2–19. https://doi.org/10.1016/j.jtice.2018.08.027.

35. Munson, B. R., Okiishi, T. H., Huebsch, W. W., & Rothmayer, A. P. (2013). Fluid mechanics. Singapore: Wiley.

36. Tsai, P., Hendrix, M. H., Dijkstra, R. R., Shui, L., & Lohse, D. (2011). Microscopic structure influencing macroscopic splash at high Weber number. Soft Matter, 7(24), 11325-11333.

37. Atencia, J., & Beebe, D. J. (2004). Controlled microfluidic interfaces. Nature, 437(7059), 648.

38. Ong, S. E., Zhang, S., Du, H., & Fu, Y. (2008). Fundamental principles and applications of microfluidic systems. Frontiers in Bioscience, 13(7), 2757–2773. https://doi.org/10.2741/2883.

39. Sebastian, V., & Arruebo, M. (2019). Microfluidic production of inorganic nanomaterials for biomedical applications. In Microfluidics for Pharmaceutical Applications (pp. 179-216). William Andrew Publishing.

40. Garstecki, P., Fuerstman, M. J., Stone, H. A., & Whitesides, G. M. (2006). Formation of droplets and bubbles in a microfluidic T-junction scaling and mechanism of break-up. Lab on a Chip, 6(3), 437-446.

41. Garstecki, P., Gitlin, I., DiLuzio, W., Whitesides, G. M., Kumacheva, E., & Stone, H. A. (2004). Formation of monodisperse bubbles in a microfluidic flow-focusing device. Applied Physics Letters, 85(13), 2649-2651.

42. Garstecki, P., Gitlin, I., DiLuzio, W., Whitesides, G. M., Kumacheva, E., & Stone, H. A. (2004). Formation of monodisperse bubbles in a microfluidic flow-focusing device. Applied Physics Letters, 85(13), 2649-2651.

43. Makgwane, P. R., & Ray, S. S. (2014). Synthesis of nanomaterials by continuous-flow microfluidics: a review. Journal of nanoscience and nanotechnology, 14(2), 1338-1363.

44. Fikiet, M. A., Khandasammy, S. R., Mistek, E., Ahmed, Y., Halámková, L., Bueno, J., & Lednev, I. K. (2018). Surface enhanced Raman spectroscopy: A review of recent applications in forensic science. Spectrochimica Acta Part A: Molecular and Biomolecular Spectroscopy, 197, 255-260.

45. C. Micsa, C. Rizea, M.I. Rusu, N.D. Becherescu-Barbu, R. Munteanu, M.V. Udrea, B. Chiricuta, A. Parau, A. Tonetto, R. Notonier, I.A. Birtoiu, C.-E.-A. Grigorescu, Surface enhanced Raman scattering in surgery and forensics,

International Conference on Transparent Optical Networks (ICTON) IEEE 2016, pp. 1–4.

46. Halouzka, V., Halouzkova, B., Jirovsky, D., Hemzal, D., Ondra, P., Siranidi, E., ... & Hrbac, J. (2017). Copper nanowire coated carbon fibers as efficient substrates for detecting designer drugs using SERS. Talanta, 165, 384-390.

47. Lafuente, M., Pellejero, I., Sebastián, V., Urbiztondo, M. A., Mallada, R., Pina, M. P., & Santamaría, J. (2018). Highly sensitive SERS quantification of organophosphorous chemical warfare agents: A major step towards the real time sensing in the gas phase. Sensors and Actuators, B: Chemical, 267, 457–466. https://doi.org/10.1016/j.snb.2018.04.058.

48. Cesaratto, A., Centeno, S. A., Lombardi, J. R., Shibayama, N., & Leona, M. (2017). A complete Raman study of common acid red dyes: application to the identification of artistic materials in polychrome prints. Journal of Raman Spectroscopy, 48(4), 601-609.

49. Zaffino, C., Ngo, H. T., Register, J., Bruni, S., & Vo-Dinh, T. (2016). “Dry-state” surface-enhanced Raman scattering (SERS): toward non-destructive analysis of dyes on textile fibers. Applied Physics A, 122(7), 707.

50. Li, M., Wu, J., Ma, M., Feng, Z., Mi, Z., Rong, P., & Liu, D. (2019). Alkyne-and nitrile-anchored gold nanoparticles for multiplex SERS imaging of

biomarkers in cancer cells and tissues. Nanotheranostics, 3(1), 113–119. https://doi.org/10.7150/ntno.30924.

51. Yaseen, T., Pu, H., & Sun, D. W. (2019). Fabrication of silver-coated gold nanoparticles to simultaneously detect multi-class insecticide residues in peach with SERS technique. Talanta, 196, 537–545. https://doi.org/10.1016/j.talanta.2018.12.030.

52. Otto, A., Mrozek, I., Grabhorn, H., & Akemann, W. (2018). Surface enhanced Raman scattering. In Compendium of Surface and Interface Analysis, 41143, pp. 661–665. https://doi.org/10.1007/978-981-10-6156-1_107 661.

53. Fan, M., Andrade, G. F., & Brolo, A. G. (2011). A review on the fabrication of substrates for surface enhanced Raman spectroscopy and their applications in analytical chemistry. Analytica chimica acta, 693(1-2), 7-25.

54. Zhu, W., Banaee, M. G., Wang, D., Chu, Y., & Crozier, K. B. (2011). Lithographically fabricated optical antennas with gaps well below 10 nm. Small, 7(13), 1761-1766.

55. Greeneltch, N. G., Blaber, M. G., Henry, A. I., Schatz, G. C., & Van Duyne, R. P. (2013). Immobilized nanorod assemblies: fabrication and understanding of large area surface-enhanced Raman spectroscopy substrates. Analytical chemistry, 85(4), 2297-2303.

56. Notarianni, M., Vernon, K., Chou, A., Liu, J., & Motta, N. (2015). Plasmonic effect of annealed gold islands for improving efficiency of organic solar cells. Advanced Device Materials, 1(1), 27-32.

57. Schlücker, S. (2014). Surface-Enhanced raman spectroscopy: Concepts and chemical applications. Angewandte Chemie International Edition, 53(19), 4756-4795.

58. Milliken, S., Fraser, J., Poirier, S., Hulse, J., & Tay, L. L. (2018). Self-assembled vertically aligned Au nanorod arrays for surface-enhanced Raman scattering (SERS) detection of Cannabinol. Spectrochimica Acta Part A: Molecular and Biomolecular Spectroscopy, 196, 222-228.

59. Lin, R., Hu, L., Wang, J., Zhang, W., Ruan, S., & Zeng, Y. J. (2018). Raman scattering enhancement of a single ZnO nanorod decorated with Ag nanoparticles: synergies of defects and plasmons. Optics letters, 43(10), 2244-2247.

60. López-lorente, A. I., Picca, R. A., Izquierdo, J., Kranz, C., Mizaikoff, B., Franco, C. Di, Valentini, A. (2018). Ion beam sputtering deposition of silver nanoparticles and TiOx / ZnO nanocomposites for use in surface enhanced vibrational spectroscopy (SERS and SEIRAS). Microchim Acta, 185(153), 1–8.

61. Yang, H., & Gijs, M. A. (2018). Micro-optics for microfluidic analytical applications. Chemical Society Reviews, 47(4), 1391-1458.

62. Lawanstiend, D., Gatemala, H., Nootchanat, S., & Eakasit, S. (2018). Microfluidic approach for in situ synthesis of nanoporous silver microstructures as on-chip SERS substrates. Sensors & Actuators: B. Chemical, 270(February), 466–474. https://doi.org/10.1016/j.snb.2018.05.051.

63. Abalde-Cela, S., Taladriz-Blanco, P., De Oliveira, M. G., & Abell, C. (2018). Droplet microfluidics for the highly controlled synthesis of branched gold nanoparticles. Scientific Reports, 8(1), 1–6. https://doi.org/10.1038/s41598-018-20754-x.

64. Huang, H., du Toit, H., Ben-Jaber, S., Wu, G., Panariello, L., Thanh, N. T. K., ... & Gavriilidis, A. (2019). Rapid synthesis of gold nanoparticles with carbon monoxide in a microfluidic segmented flow system. Reaction Chemistry & Engineering, 4(5), 884-890.

65. Le Ru, E., & Etchegoin, P. (2008). Principles of Surface-Enhanced Raman Spectroscopy: and related plasmonic effects. Elsevier.

66. Günther, A., Jhunjhunwala, M., Thalmann, M., Schmidt, M. A., & Jensen, K. F. (2005). Micromixing of miscible liquids in segmented gas− liquid flow. Langmuir, 21(4), 1547-1555.

67. Ji, X., Song, X., Li, J., Bai, Y., Yang, W., & Peng, X. (2007). Size control of gold nanocrystals in citrate reduction: the third role of citrate. Journal of the American Chemical Society, 129(45), 13939-13948.

68. Manno, R., Sebastian, V., Mallada, R., & Santamaria, J. (2019). 110th Anniversary: Nucleation of Ag Nanoparticles in Helical Microfluidic Reactor. Comparison between Microwave and Conventional Heating. Industrial & Engineering Chemistry Research, 58(28), 12702-12711.

69. Kulkarni, A. A., & Sebastian Cabeza, V. (2017). Insights in the diffusion controlled interfacial flow synthesis of Au nanostructures in a microfluidic system. Langmuir, 33(50), 14315-14324.

70. Sebastian Cabeza, V., Kuhn, S., Kulkarni, A. A., & Jensen, K. F. (2012). Size-controlled flow synthesis of gold nanoparticles using a segmented flow microfluidic platform. Langmuir, 28(17), 7007-7013.

71. Zhao, B., MacMinn, C. W., & Juanes, R. (2016). Wettability control on multiphase flow in patterned microfluidics. Proceedings of the National Academy of Sciences, 113(37), 10251-10256.

72. Gale, B. K., Jafek, A. R., Christopher, J. L., & Goenner, B. L. (2018). A Review of Current Methods in Microfluidic Device Fabrication and Future Commercialization Prospects. Inventions, 3(60), 1–25. https://doi.org/10.3390/inventions3030060.

73. Ontiveros, F., & McDowell, J. R. (2016). Ultra-Thin Microfluidic Devices Built via Thermal Lamination.

74. Faustino, V., Catarino, S. O., Lima, R., & Minas, G. (2016). Biomedical microfluidic devices by using low-cost fabrication techniques: A review. Journal of biomechanics, 49(11), 2280-2292.

75. Waheed, S., Cabot, J. M., Macdonald, N. P., Lewis, T., Guijt, R. M., Paull, B., & Breadmore, M. C. (2016). 3D printed microfluidic devices: enablers and barriers. Lab on a Chip, 16(11), 1993-2013.

76. Xi, Y., Zhang, W., Fan, Z., Ma, Q., Wang, S., Ma, D., ... & Zhang, Y. (2018). A facile synthesis of silicon nanowires/micropillars structure using lithography and metal-assisted chemical etching method. Journal of Solid State Chemistry, 258, 181-190.

77. Kinahan, D. J., Julius, L. A., Schoen, C., Dreo, T., & Ducrée, J. (2018). Automated DNA purification and multiplexed lamp assay preparation on a centrifugal microfluidic “Lab-on-a-Disc” platform. IEEE Micro Electro Mechanical Systems, 1134-1137.

78. Pinto, V., Sousa, P., Cardoso, V., & Minas, G. (2014). Optimized SU-8 processing for low-cost microstructures fabrication without cleanroom facilities. Micromachines, 5(3), 738-755.

79. Wiedemeier, S., Römer, R., Wächter, S., Staps, U., Kolbe, C., & Gastrock, G. (2017). Precision moulding of biomimetic disposable chips for droplet-based applications. Microfluidics and Nanofluidics, 21(11), 167.

80. Weerakoon-Ratnayake, K. M., O'Neil, C. E., Uba, F. I., & Soper, S. A. (2017). Thermoplastic nanofluidic devices for biomedical applications. Lab on a Chip, 17(3), 362-381.

81. Li, D., Yu, H., Pu, Z., Lai, X., Sun, C., Wu, H., & Zhang, X. (2020). Flexible Microfluidics for Wearable Electronics. Flexible and Wearable Electronics for Smart Clothing, 213-235.

82. Shang, L., Cheng, Y., & Zhao, Y. (2017). Emerging droplet microfluidics. Chemical reviews, 117(12), 7964-8040.

83. Au, A. K., Huynh, W., Horowitz, L. F., & Folch, A. (2016). 3D-printed microfluidics. Angewandte Chemie International Edition, 55(12), 3862-3881.

84. Kadimisetty, K., Mosa, I. M., Malla, S., Satterwhite-Warden, J. E., Kuhns, T. M., Faria, R. C., ... & Rusling, J. F. (2016). 3D-printed supercapacitor-powered electrochemiluminescent protein immunoarray. Biosensors and Bioelectronics, 77, 188-193.

85. Urrios, A., Parra-Cabrera, C., Bhattacharjee, N., Gonzalez-Suarez, A. M., Rigat-Brugarolas, L. G., Nallapatti, U., ... & Folch, A. (2016). 3D-printing of transparent bio-microfluidic devices in PEG-DA. Lab on a Chip, 16(12), 2287-2294.

86. He, Y., Wu, Y., Fu, J. Z., Gao, Q., & Qiu, J. J. (2016). Developments of 3D printing microfluidics and applications in chemistry and biology: a review. Electroanalysis, 28(8), 1658-1678.

87. Sugioka, K., Xu, J., Wu, D., Hanada, Y., Wang, Z., Cheng, Y., & Midorikawa, K. (2014). Femtosecond laser 3D micromachining: a powerful tool for the fabrication of microfluidic, optofluidic, and electrofluidic devices based on glass. Lab on a Chip, 14(18), 3447-3458.

88. Moolman, M. C., Huang, Z., Krishnan, S. T., Kerssemakers, J. W., & Dekker, N. H. (2013). Electron beam fabrication of a microfluidic device for studying submicron-scale bacteria. Journal of nanobiotechnology, 11(1), 12.

89. Isobe, G., Kanno, I., Kotera, H., & Yokokawa, R. (2012). Perfusable multi-scale channels fabricated by integration of nanoimprint lighography (NIL) and UV lithography (UVL). Microelectronic Engineering, 98, 58-63.

90. Jo, H., Haberkorn, N., Pan, J. A., Vakili, M., Nielsch, K., & Theato, P. (2016). Fabrication of chemically tunable, hierarchically branched polymeric nanostructures by multi-branched anodic aluminum oxide templates. Langmuir, 32(25), 6437-6444.

91. Dupont, D., & Alexandre, G. (2011). Rapport de Stage. Rapport de stage LBMS (Vol. 1). https://doi.org/10.2143/REA.28.1.505102.

92. Cai, G., Xue, L., Zhang, H., & Lin, J. (2017). A review on micromixers. Micromachines, 8(9). https://doi.org/10.3390/mi8090274

93. Javaid, M. U., Cheema, T. A., & Park, C. W. (2017). Analysis of passive mixing in a serpentine microchannel with sinusoidal side walls. Micromachines, 9(1), 1–15. https://doi.org/10.3390/mi9010008

94. Anna, S. L., Bontoux, N., & Stone, H. A. (2003). Formation of dispersions using “flow focusing” in microchannels. Applied physics letters, 82(3), 364-366.

95. Ong, S. E., Zhang, S., Du, H., & Fu, Y. (2008). Fundamental principles and applications of microfluidic systems. Frontiers in Bioscience, 13(7), 2757-2773.

96. Tropea, C., & Yarin, A. L. (2007). Springer handbook of experimental fluid mechanics. Springer Science & Business Media.

97. Tabeling, P. (2004). Slip phenomena at liquid-solid interfaces. Comptes Rendus Physique, 5(5), 531-537.

98. Tian, Z., Ge, X., Wang, Y., & Xu, J. (2019). Nanoparticles and Nanocomposites With Microfluidic Technology. In Polymer-Based Multifunctional Nanocomposites and Their Applications (pp. 1-33). Elsevier.

99. Dressaire, E., & Sauret, A. (2017). Clogging of microfluidic systems. Soft Matter, 13(1), 37-48.

100. Köhler, J. M., & Cahill, B. P. (2014). Micro-Segmented Flow. In Materials Science Forum.

101. Schroën, K., Ferrando, M., Lamo-Castellví, D., Sahin, S., & Güell, C. (2016). Linking findings in microfluidics to membrane emulsification process design: the importance of wettability and component interactions with interfaces. Membranes, 6(2), 26.

102. Nourafkan, E., & Alamdari, A. (2014). Study of effective parameters in silver nanoparticle synthesis through method of reverse microemulsion. Journal of Industrial and Engineering Chemistry, 20(5), 3639-3645.

103. Paramelle, D., Sadovoy, A., Gorelik, S., Free, P., Hobley, J., & Fernig, D. G. (2014). A rapid method to estimate the concentration of citrate capped silver nanoparticles from UV-visible light spectra. Analyst, 139(19), 4855-4861.

104. Xu, L., Peng, J., Yan, M., Zhang, D., & Shen, A. Q. (2016). Droplet synthesis of silver nanoparticles by a microfluidic device. Chemical Engineering and Processing: Process Intensification, 102, 186-193.

105. Lu, L., & An, X. (2015). Silver nanoparticles synthesis using H2 as reducing agent in toluene–supercritical CO2 microemulsion. The Journal of Supercritical Fluids, 99, 29-37.

106. Nightingale, A. M., Phillips, T. W., Bannock, J. H., & De Mello, J. C. (2014). Controlled multistep synthesis in a three-phase droplet reactor. Nature communications, 5(1), 1-8.

107. V. S. Cabeza, S. Kuhn, A. A. Kulkarni, and K. F. Jensen, “Size-Controlled Flow Synthesis of Gold Nanoparticles Using a Segmented Flow Micro fl uidic Platform,” Langmuir, vol. 28, pp. 7007–7013, 2012.

108. Njoki, P. N., Lim, I. I. S., Mott, D., Park, H. Y., Khan, B., Mishra, S., ... & Zhong, C. J. (2007). Size correlation of optical and spectroscopic properties for gold nanoparticles. The Journal of Physical Chemistry C, 111(40), 14664-14669.

109. Scarabelli, L., Coronado-Puchau, M., Giner-Casares, J. J., Langer, J., & Liz-Marzan, L. M. (2014). Monodisperse gold nanotriangles: size control, large-scale self-assembly, and performance in surface-enhanced Raman scattering. ACS nano, 8(6), 5833-5842.

110. Grzelczak, M., Pérez-Juste, J., Mulvaney, P., & Liz-Marzán, L. M. (2008). Shape control in gold nanoparticle synthesis. Chemical Society Reviews, 37(9), 1783-1791.

111. Enders, A., Siller, I. G., Urmann, K., Hoffmann, M. R., & Bahnemann, J. (2019). 3D printed microfluidic mixers—A comparative study on mixing unit performances. Small, 15(2), 1804326.

112. Tserkezis, C., Taylor, R. W., Beitner, J., Esteban, R., Baumberg, J. J., & Aizpurua, J. (2014). Optical response of metallic nanoparticle heteroaggregates with subnanometric gaps. Particle & Particle Systems Characterization, 31(1), 152-160.

113. Sun, L., Luan, W., Shan, Y., & Tu, S. T. (2012). One-step synthesis of monodisperse Au–Ag alloy nanoparticles in a microreaction system. Chemical engineering journal, 189, 451-455.

114. Wu, L., Liu, X., Zhao, Y., & Chen, Y. (2017). Role of local geometry on droplet formation in axisymmetric microfluidics. Chemical Engineering Science, 163, 56-67.

115. Phatangare, A. B., Dhole, S. D., Dahiwale, S. S., & Bhoraskar, V. N. (2018). Ultra-high sensitive substrates for surface enhanced Raman scattering, made of 3 nm gold nanoparticles embedded on SiO2 nanospheres. Applied Surface Science, 441, 744-753.

116. Hu, X., Wang, T., Wang, L., & Dong, S. (2007). Surface-enhanced Raman scattering of 4-aminothiophenol self-assembled monolayers in sandwich structure with nanoparticle shape dependence: off-surface plasmon resonance condition. The Journal of Physical Chemistry C, 111(19), 6962-6969.

APPENDICES

APPENDIX A

PDMS/glass Microfluidic Devices

A.1. Materials and methods.

A.1.2. Droplet generation control.

Before starting with the synthesis of noble metal nanoparticles, a series of tests was carried out only with a water-oil system to know the flow conditions at which the generation of droplets in a dripping regime remains stable and controllable.

The device design and methodology of fabrication were the same reported in section 3.1.1 as well as the setup employed in section 4.1.1.

For droplet generation experiments, water and oil were flowed at different conditions until observe a controllable and stable droplet formation. MilliQ water and Silicone Oil 10 cSt were employed. Table A1 resume the flow conditions tested, where Qoil corresponds to silicon oil flow rate and QwT is the total water flow rate.

Table A1. Droplet generation flow conditions.

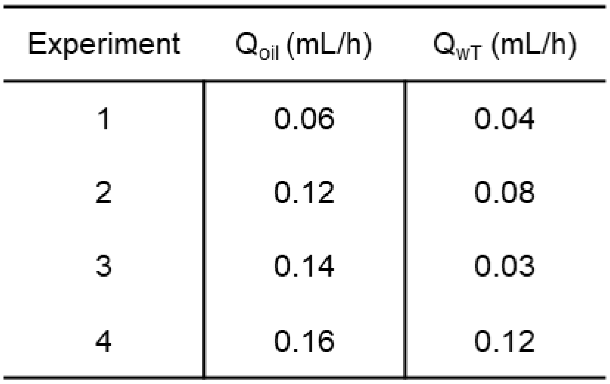

Experiment	Q_{oil} (mL/h)	Q_{wT} (mL/h)
1	0.06	0.04
2	0.12	0.08
3	0.14	0.03
4	0.16	0.12

A.1.3. Coalescence removal.

To remove the coalescence problem presented between water droplets, Span 80 surfactant was dissolved in the oil phase at different concentrations (Table A2). The total flow rate was fixed at 0.28 mL/h (Experiment 2). To prepare each suspension, the necessary Span 80 quantity was added to silicone oil and then, was sonicated for 5 min.

Table A2. Span 80 concentrations tasted.

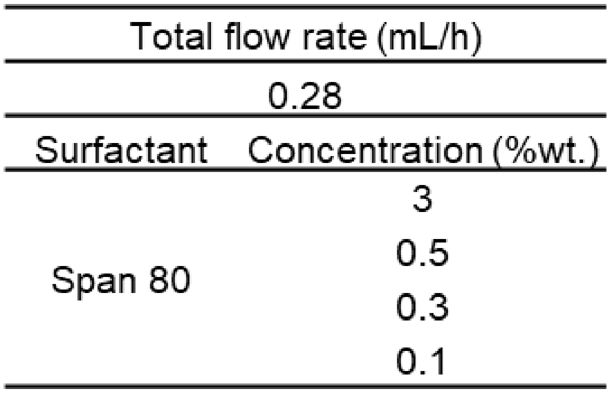

Total flow rate (mL/h)	
0.28	
Surfactant	Concentration (%wt.)
Span 80	3
	0.5
	0.3
	0.1

A.2. Results and Discussion.

A.2.1. Droplet generation control.

The flow rates conditions in Experiment 1 lead to water slug formation, as Figure A1 shows.

Figure A1. Squeezing regime forming aqueous slug formation.

At this flow rate, the oil fluid velocity was not fast enough to pass through the microchannel junction, being obstructed by the passage of the dispersed phase (water)[1]. In consequence, a pressure gradient in oil across the enlarging slug is built up as the space between the liquid interface and the channel walls decreases[2]. When the pressure gradient is sufficiently large to overcome the pressure inside the dispersed droplet, the interface is “squeezed” to deform and necks into a slug[3]. This squeezing regime occurs when the continuous phase pressure increase, breaking up the dispersed phase in slugs.

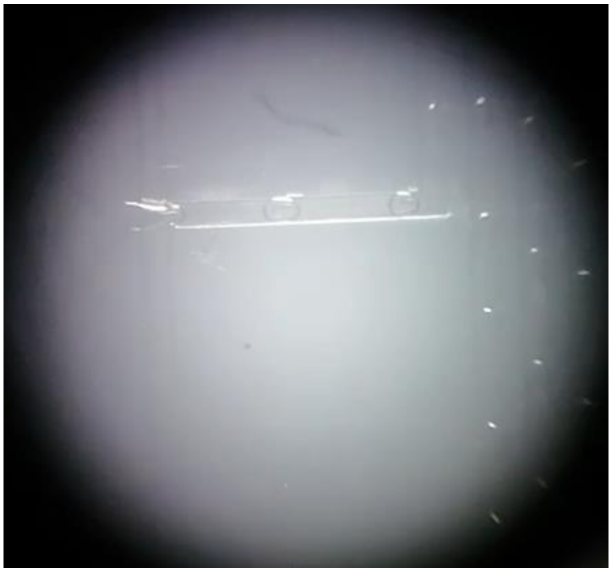

Figure A2. Dripping regime forming aqueous droplets.

However, when the flow rates were slightly increased in Experiment 2, the generation of homogeneous droplets was observed (Figure A2). This due to the viscous forces and viscous shear stress related, drag the liquid interface to rupture, dominating over interfacial tension effects, stabilizing the emerging droplet against breakup[4].

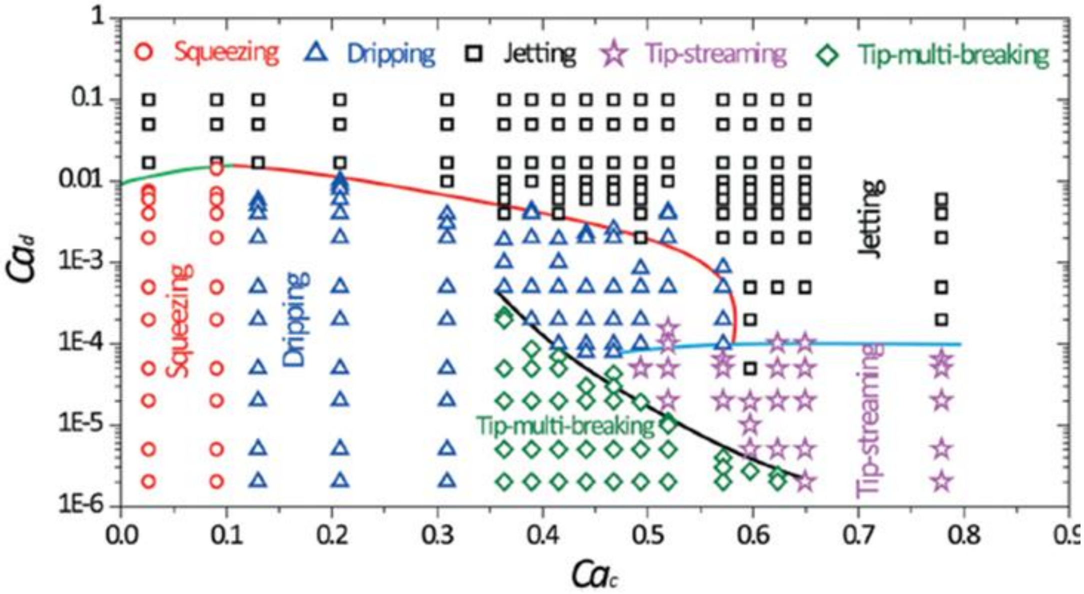

Figure A3. Regime diagram in microfluidic flow-focusing devices.

This transition between squeezing and dripping regime is domine by capillary number as Zhu *et al.* reported in their research work[4]. In Figure A3, they report a "Regime Diagram" where it is depends to the capillary number changes, the regime that will domain in the droplet formation, transition that was controlled only duplicating the flow rates in Experiment 2.

On the other hand, when the flow rates continuous grow (Experiment 3 and 4), the continuous phase pressure increased, going in opposite direction to the aqueous flows. These backflow problems generated fluid lick in the PEEK tubing connections, as we can see in Figure A4.

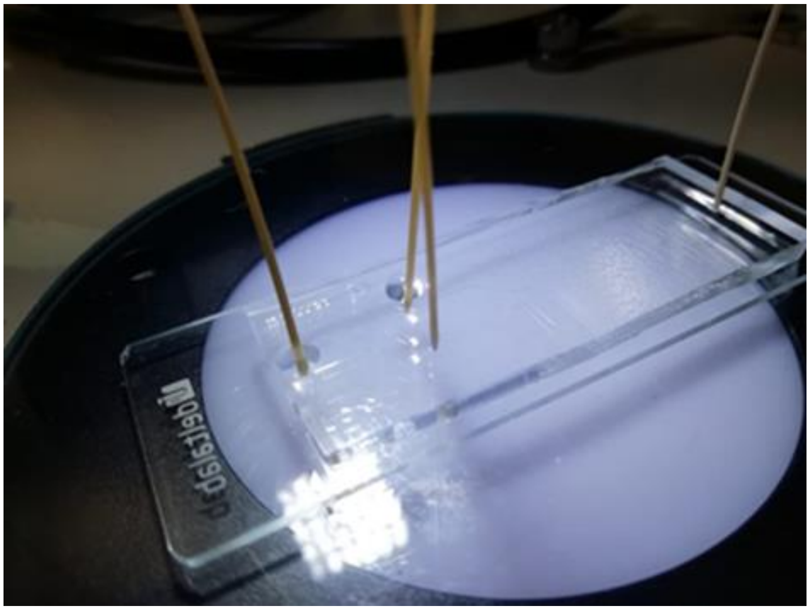

Figure A4. Leak problem in PDMS/glass device due to backflow.

For the observations, we decide to proceed with flow rate conditions in Experiment 3. However, in Figure A5 is showed that the droplet formation was not stable during time through all the device because they started to coalesce and grow, making not reproducible experiment.

Figure A5. Aqueous droplet coalescence through microchannels.

Due to this, it was decided to work with a total flow rate equal to that of Experiment 3 for the microfluidic synthesis of noble metal nanoparticles.

A.2.2. Coalescence removal.

To avoid the coalescence problem, the use of Span 80 as surfactant following Table A2 conditions was employed to try to reduce the electrostatic interaction between water droplets before to start to synthesize.

At Span 80 concentration of 3% and 0.5%wt. an emulsion was formed, producing a clogging effect in the microchannels and, as in batch chemical pipes, the obstruction of the flow of both phases causes a disruption in the velocities of the fluids, nothing favorable for the chemical synthesis (Figure A6).

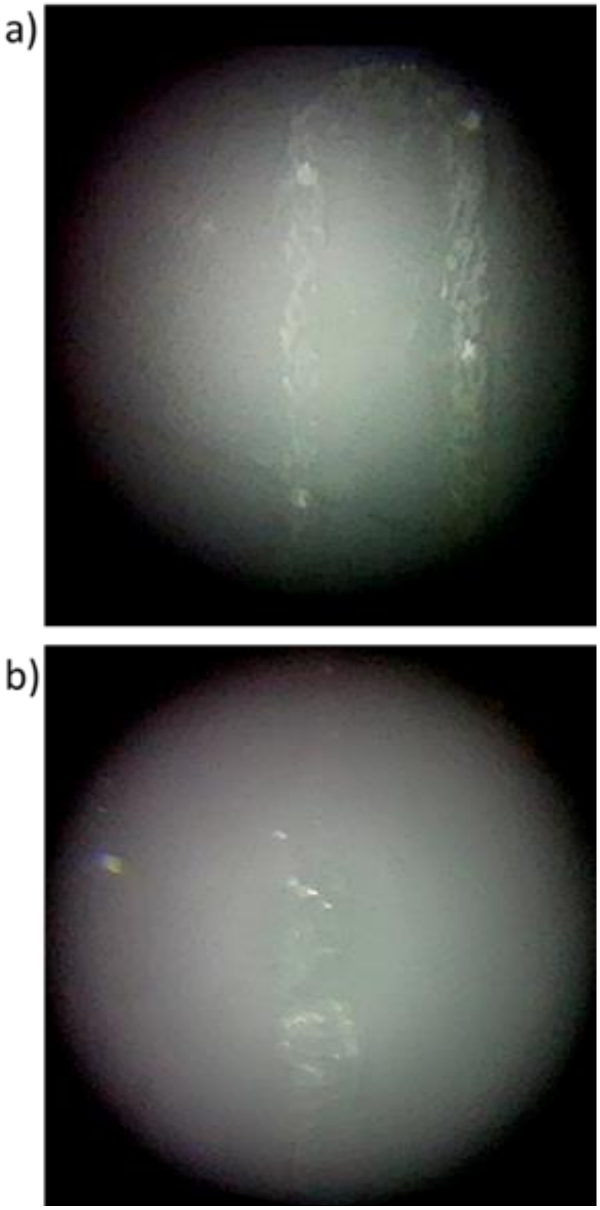

Figure A6. Microchannels clogged. a) Clogging problem at Span 80 3% wt. 1. b) Clogging problem in at Span 80 0.5% wt.

However, as in Figure A6b, the clogging effect decrease but not enough to maintain the droplet formation, in contrast with Span 80 0.3% wt that permitted the control in droplets and avoided the droplet coalescence, as is showed below.

Figure A7. Stable droplet formation at Span 80 3% wt.

On the other hand, the use of Span 80 0.1%wt. was to dilute to produce some interaction and avoid the coalescence, observing the same behavior without surfactant. However, any figure was presented due to the velocity of the droplets that the conventional camera did not capture as faster as they movement.

REFERENCES

1. M. Nightingale et al., “A stable droplet reactor for high temperature nanocrystal synthesis,” Lab Chip, vol. 11, no. 7, pp. 1221–1227, 2011.

2. Zhu, P., & Wang, L. (2017). Passive and active droplet generation with microfluidics: a review. Lab on a Chip, 17(1), 34-75.

3. P. Garstecki, I. Gitlin, W. DiLuzio, G. M. Whitesides, E. Kumacheva and H. A. Stone Appl. Phys. Lett., 2004, 85,2649–2651.

4. De Menech, M., Garstecki, P., Jousse, F., & Stone, H. A. (2008). Transition from squeezing to dripping in a microfluidic T-shaped junction. journal of fluid mechanics, 595, 141-161.

5. Zhu, P., Kong, T., Kang, Z., Tian, X., & Wang, L. (2015). Tip-multi-breaking in capillary microfluidic devices. Scientific reports, 5(1), 1-8.

APPENDIX B

B.1. Materials and Methods

B.1.2. Design and Microfabrication of Microfluidic Tubing Reactor

A co-flow tubing reactor was fabricated using a translucent PTFE tubing with I.D. 0.8 mm and O.D. 3.25 mm as mean tube and two SiO_2 capillaries with I.D. 100 μm and O.D. 365 μm Ø were used as inlets. The fabrication of these tubing reactors was realized punctured the PTFE tube for insert the capillaries on it and then, for avoid some licking problem, these PTFE-SiO_2 capillary join were glued with industrial epoxy glue.

For realize the Ag and Au synthesis in a separate way, two tubing reactors were fabricated. For Ag tubing reactor, the length of the tube was 1 m, getting 0.5 mL of reactor volume. About the Au tubing reactor, the length of the tube was 1.90 m, getting 0.95 mL of reactor volume. In bout cases, the outlet was the same PTFE tube at the end of the reactor.

B.2. Results and Discussion

B.2.1. Microfluidic Ag and Au synthesis

This geometry favors the dripping regime, producing very stable droplets even without surfactant[1], as we can see in Figure B1.

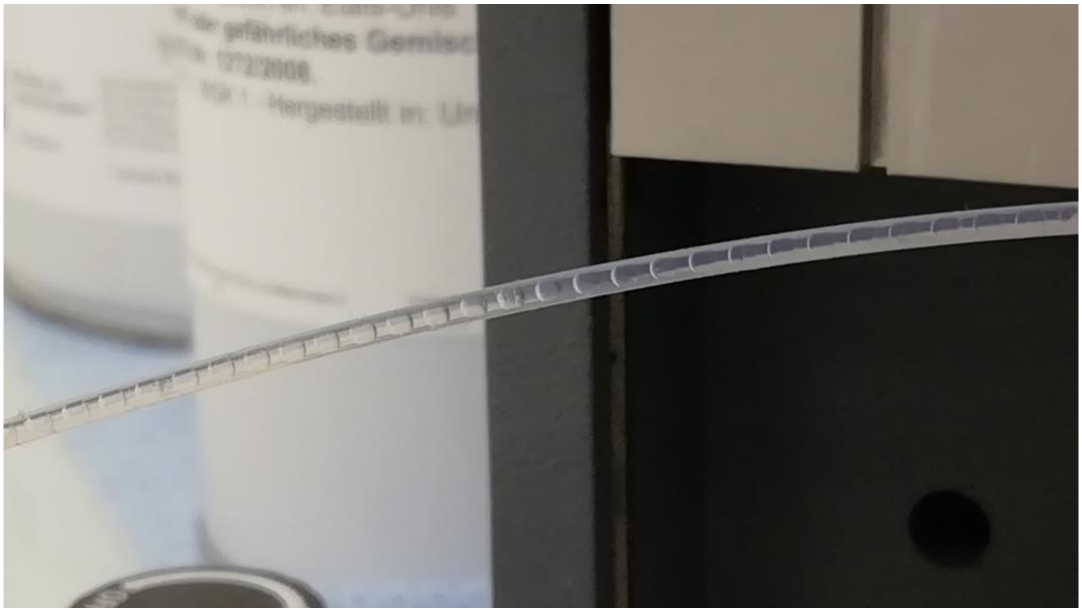

Figure B1. Stable droplet flow through the microfluidic tubing reactor.

For Ag NPs synthesis, Table B1 shows the flow conditions used where one syringe contained 1 mL of MilliQ water, 3 mL of Na_3Cit 5 mM and 1 mL of

$AgNO_3$ 1mM and the other syringe contained 5 mL of $NaBH_4$ 8 mM and Table B2 shows the flow conditions for Au microfluidic synthesis, where one syringe contained 5 mL of $HAuCl_4$ 0.25 mM and the other one contained 5 mL of Na_3Cit 34.5 mM. The products were collected and separated from the oil phase to their subsequent UV-Vis analysis.

Table B1. Flow rate conditions for microfluidic Ag nanoparticles synthesis using tubing microreactor.

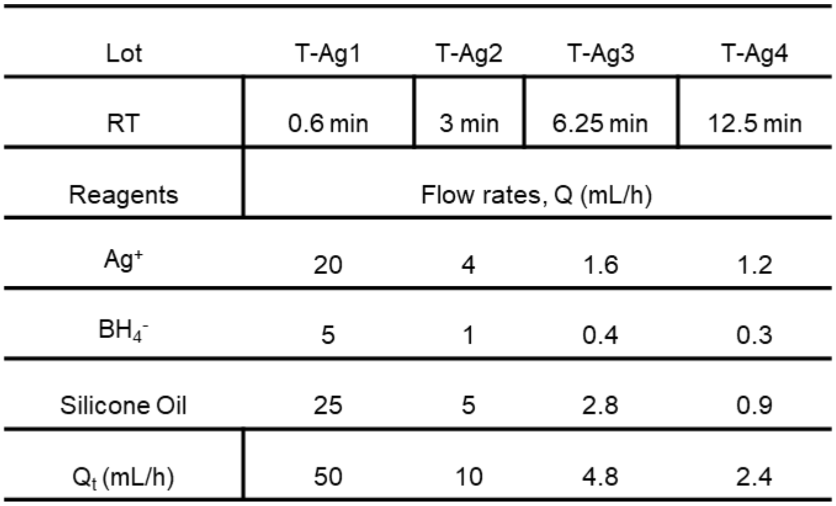

Lot	T-Ag1	T-Ag2	T-Ag3	T-Ag4
RT	0.6 min	3 min	6.25 min	12.5 min
Reagents	Flow rates, Q (mL/h)			
Ag^+	20	4	1.6	1.2
BH_4^-	5	1	0.4	0.3
Silicone Oil	25	5	2.8	0.9
Q_t (mL/h)	50	10	4.8	2.4

Table B2. Flow rate conditions for microfluidic Au nanospheres synthesis using tubing microreactor.

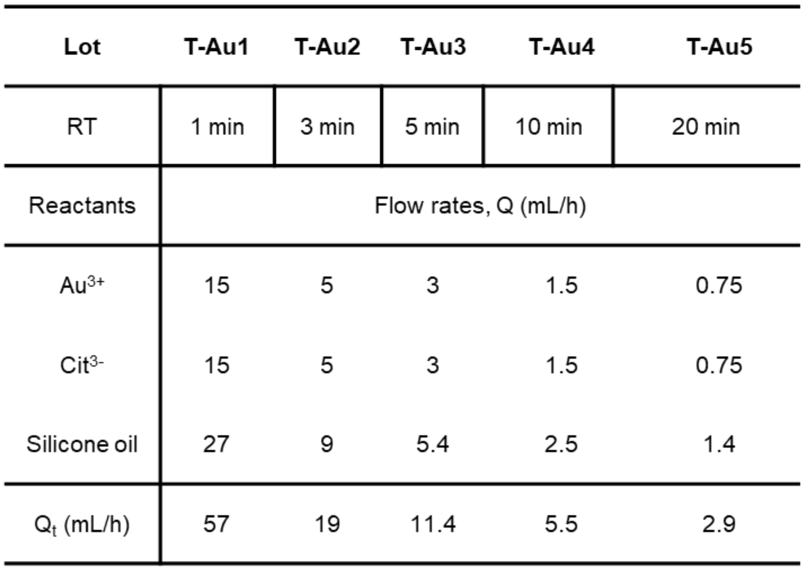

Lot	T-Au1	T-Au2	T-Au3	T-Au4	T-Au5
RT	1 min	3 min	5 min	10 min	20 min
Reactants	Flow rates, Q (mL/h)				
Au^{3+}	15	5	3	1.5	0.75
Cit^{3-}	15	5	3	1.5	0.75
Silicone oil	27	9	5.4	2.5	1.4
Q_t (mL/h)	57	19	11.4	5.5	2.9

We can observe that, as increasing the residence time, the Ag concentration decreases (Table B2). That is why, during 0.6 and 3 minutes of residence time, the better Ag production was observed than in residence times of 6.25 and 12.5 minutes (Figure B2). This could be related to the introduction of less and less reducing agent at the system because, for the best droplet production in the reactor, a 4:1 ratio was maintained in the flows rates of the reagents.

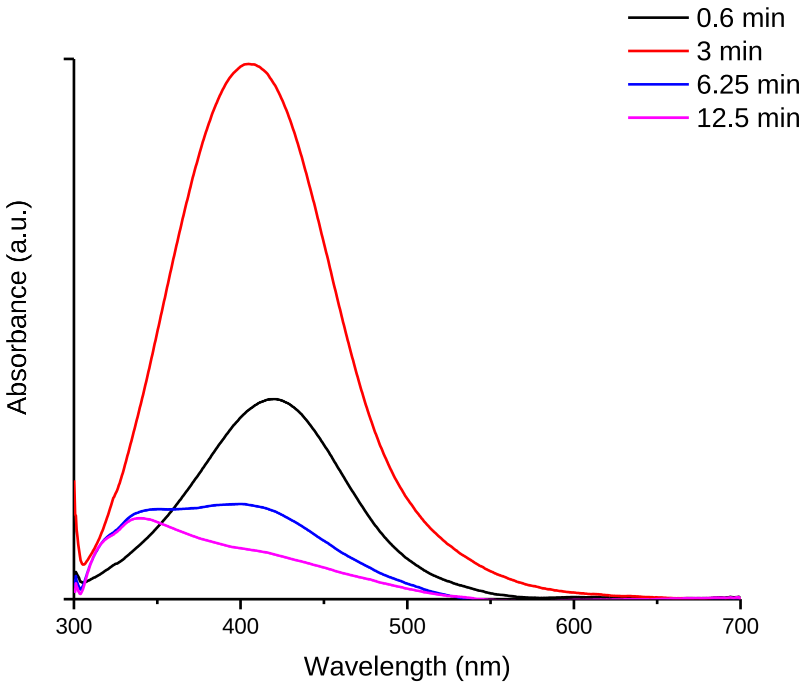

Figure B2. UV-Vis spectra of Ag nanospheres spectra obtained with tubing microreactor at Table 3 conditions.

This same behavior was presented in microfluidic Au NPs synthesis (Figure B3). This tendency might be related with growth mechanisms[1-3] and microfluidic flow condition ratios[4-6]; however, we could not investigate more about this due to we faced a clogging problem just in the capillaries tips as we can observe in Figure X.

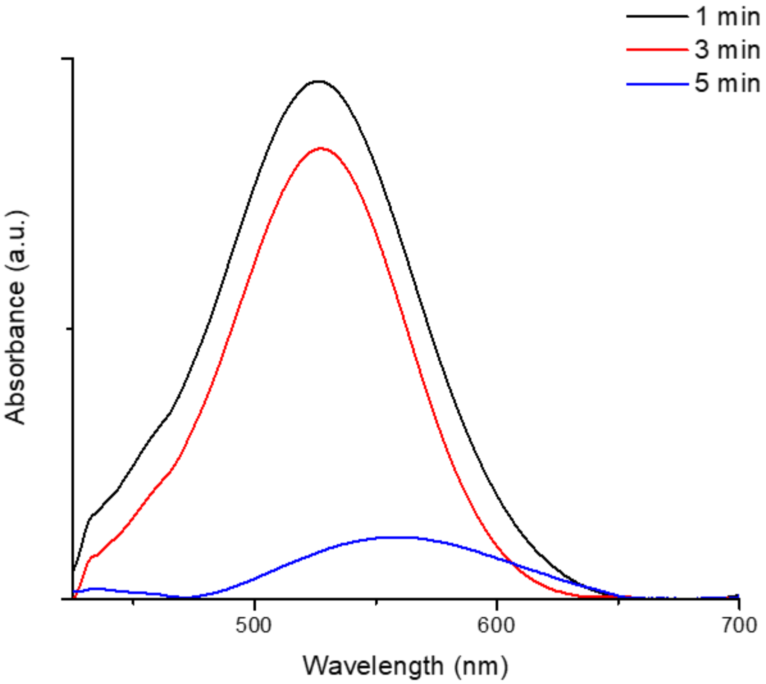

Figure B3. UV-Vis spectra of Au nanospheres spectra obtained with tubing microreactor at Table 6 conditions.

This clogging problem affected the nanoparticles synthesis in terms of internal fluids flow, producing a non-homogenous droplet generation. Also, to replace these capillaries, meant fabricate others microfluidics reactors suggesting huge variations between them.

Due to that, the design used in 3.1.3 section was preferred. The clogging problem never was solved, however, this design permitted to clean the capillaries by removing the PEEK plug just in front of the Tee junction.

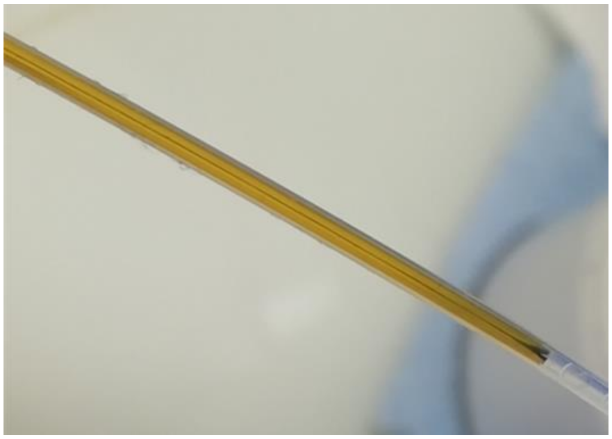

Figure B4. Clogging effect on the capillaries tips.

REFERENCES

1. Wang, B., Prinsen, P., Wang, H., Bai, Z., Wang, H., Luque, R., & Xuan, J. (2017). Macroporous materials: microfluidic fabrication, functionalization and applications. Chemical Society Reviews, 46(3), 855-914.

2. CRIADO, C. L., & RESÉNDEZ, R. M. (2008). Formación de par mación de par mación de partículas nanométr tículas nanométr tículas nanométricas en soluciones sobresaturadas. CIENCIA UANL, 11(3), 244.

3. Mer, V. K. L. (1952). Nucleation in phase transitions. Industrial & Engineering Chemistry, 44(6), 1270-1277.

4. Kang, K. K., Lee, B., & Lee, C. S. (2019). Recent progress in the synthesis of inorganic particulate materials using microfluidics. Journal of the Taiwan Institute of Chemical Engineers, 98, 2-19.

5. Paramelle, D., Sadovoy, A., Gorelik, S., Free, P., Hobley, J., & Fernig, D. G. (2014). A rapid method to estimate the concentration of citrate capped silver nanoparticles from UV-visible light spectra. Analyst, 139(19), 4855-4861.

6. Boufi, S., Vilar, M. R., Ferraria, A. M., & do Rego, A. M. B. (2013). In situ photochemical generation of silver and gold nanoparticles on chitosan. Colloids and Surfaces A: Physicochemical and Engineering Aspects, 439, 151-158.

Microfluidics and Surface-Enhanced Raman Spectroscopy: A Perfect Match for New Analytical Tools

Gustavo Ochoa-Vazquez, Boris Kharisov, Ana Arizmendi-Morquecho, Anaïs Cario, Cyril Aymonier, Samuel Marre, and Israel López

***Abstract*— In this perspective article, we emphasize the combination of Surface-Enhanced Raman Spectroscopy (SERS) and Microfluidic devices. SERS approaches have been widely studied and used for multiple applications including trace molecules detection, *in situ* analysis of biological samples and monitoring or, all of them with good results, however still with limitations of the technique, for example regarding with improved precision and reproducibility. These implications can be overcome by microfluidic approaches. The resulting coupling Microfluidics – SERS (MF-SERS) has recently gained increasing attention by creating thundering opportunities for the analytical field. For this purpose, we introduce some of the strategies developed to implement SERS within microfluidic reactor along with a brief overview of the most recent MF-SERS applications for biology, health and environmental concerns. Eventually, we will discuss future research opportunities of such systems.**

***Index Terms*— Microfluidics, surface-enhanced Raman spectroscopy, lab on a chip, *in situ* characterization.**

I. INTRODUCTION

IN THE last decades, Raman spectroscopy has gained increasing attention as an analytical tool, being conventionally used to provide researchers with precious data for solving problematics in various topics such as environment, safety, biology and healthcare. This technique collects the inelastic dispersion with respect to an incident wavelength, allowing monitoring the vibrational modes of the molecules or material investigated. Due to the coupling to microscope, Raman spectroscopy can be used to perform (bio)chemical imaging at higher spatial resolution (less than 200 nm) that what can be typically obtained with Infrared spectroscopy [1]. However, this characterization tool is known to have a low sensitivity due to weak Raman scattering, which is one of the major problems associated with this technique. Therefore, for some specific applications, this has pushed researchers to consider one technique now widely used in Raman spectroscopy: The Surface-Enhanced Raman Scattering (SERS). This is a surface approach that enhances Raman scattering (the gain can reach a factor up to 10^{10}, thus allowing the detection of trace molecules) due to the interactions between the investigated molecules and different nanostructured substrates constituted of noble metals generating localized surface plasmons and hot spots in between metals nanoparticles [2]. The fabrication of carefully-designed SERS substrates has been widely investigated; however, various challenges still exist in SERS, limiting its adoption by a wider scientific community, namely: the substrates fabrication reproducibility [3], the difficulty of realizing field measures and the high cost of analysis represent the most current problems [4]. With the purpose of addressing these limitations, the scientific community has look towards microscale processes through the use of microfluidics fundamentals.

Microfluidics is the scientific field that studies the behavior of the fluids and their control at microscale using microchannels displaying dimensions in the order of tens to hundreds of μm [5]. The design, fabrication and use of microfluidic devices have permitted to solve some problems related to the SERS technique, thanks to high precision and reproducibility in the synthetic and/or analytical parameters [6], leading to the so-called MF-SERS approaches.

Over the past 10 years, an increasing number of studies have reported and reviewed the use of MF-SERS to miniaturize the analytical systems and to enhance their reproducibility [7]–[11] (Figure 1). The applications of such systems are

Manuscript received February 28, 2019; revised September 2, 2019; accepted September 8, 2019. Date of publication September 23, 2019; date of current version October 18, 2019. This work was supported by the European Research Council (ERC) through the European Union's Horizon 2020 Research and Innovation Program under Grant 725100 (project Big Mac). The work of G. Ochoa-Vazquez was supported by the Consejo Nacional de Ciencia y Tecnología of Mexico (CONACYT) through the Ph.D. Research Scholarship under Grant 713466. *(Corresponding authors: Samuel Marre; Israel López.)*

G. Ochoa-Vazquez is with Universidad Autónoma de Nuevo León (UANL), Facultad de Ciencias Químicas (FCQ), Centro de Investigación en Biotecnología y Nanotecnología (CIBYN), Apodaca 66629, Mexico, and also with CNRS, Université Bordeaux, Bordeaux INP, ICMCB, UMR 5026, F-33600 Pessac, France.

B. Kharisov is with Universidad Autónoma de Nuevo León (UANL), Facultad de Ciencias Químicas (FCQ), Centro de Laboratorios Especializados (CELAES), San Nicolás de los Garza 66455, Mexico.

A. Arizmendi-Morquecho is with the Centro de Investigación en Materiales Avanzados, S. C. (CIMAV), Unidad Monterrey, Apodaca 66600, Mexico.

A. Cario, C. Aymonier, and S. Marre are with CNRS, Université Bordeaux, Bordeaux INP, ICMCB, UMR 5026, F-33600 Pessac, France (e-mail: samuel.marre@icmcb.cnrs.fr).

I. López is with Universidad Autónoma de Nuevo León (UANL), Facultad de Ciencias Químicas (FCQ), Centro de Investigación en Biotecnología y Nanotecnología (CIBYN), Apodaca 66629, Mexico (e-mail: israel.lopezhr@uanl.edu.mx).

Digital Object Identifier 10.1109/TNB.2019.2943078

Continuous Segmented-Flow Synthesis of Ag and Au Nanoparticles Using a Low Cost Microfluidic PTFE Tubing Reactor

Gustavo Ochoa-Vazquez, Boris Kharisov, Ana Arizmendi-Morquecho, Anaïs Cario,
Cyril Aymonier, Samuel Marre, and Israel López

***Abstract*—We present in here a simple and low cost continuous segmented-flow process for the synthesis of Ag and Au spherical-shaped nanoparticles. Different residence times (RT) were used to perform the nanoparticle synthesis, observing that at low RT, the Ag nanoparticles production, which uses a fast reduction reaction with $NaBH_4$, is improved due to an enhancement in the mixing of the reactants. However, the flow conditions have an opposite effect in the case of Au nanoparticles synthesis. Indeed, since the chemical reduction process (Turkevich method) exhibit a much slower kinetics, high RT (low flowrates) improve the synthesis yield and the quality of the nanoparticles. The Ag and Au nanoparticles were characterized by UV-Vis spectrophotometry (UV-Vis) and Transmission Electron Microscopy (TEM). The Ag spherical-shaped nanoparticles presented a LSPR at 400 nm (size $\approx$ 4 nm), while the synthesized Au nanoparticles exhibit LSPR and sizes in the range 520 - 550 nm and 14 - 17 nm, respectively.**

***Index Terms*—Ag nanoparticles, Au nanoparticles, Flow synthesis, Microfluidics, Microfluidic synthesis, Noble metal nanoparticles.**

I. INTRODUCTION

IN THE last decade, Ag and Au nanoparticles (NPs) have been widely used in photonics [1], electronics [2], biomedicine [3] and catalysis [4] as well as in surface-enhanced Raman spectroscopy (SERS) for the design of nanostructured substrates [5] and chemical and biological sensors [6] thanks to their physical, chemical, optical and size-dependent properties [2].

Different synthesis methods have been employed to obtain these materials with distinct morphologies and sizes among which are electrochemical processes [7], photoreduction [8] or bio-assisted synthesis [9]. These approaches have permitted the obtention of several morphologies including nanospheres [10], nanorods [11] and nanotriangles [12] with sizes ranging from 4 nm to 100 nm [13]. Nevertheless, the most employed synthesis method remains the chemical reduction of metal precursors, which lead to the faster kinetics towards nanoparticle production [14]. Commonly, sodium borohydride ($NaBH_4$) is used as reducing agent in the Au and Ag nanoparticle synthesis for its potential reduction, while sodium citrate ($Na_3C_6H_5O_7{\cdot}2H_2O$ - Na_3Cit) is employed to stabilize the growth of the nanoparticles, producing spherical-shaped nanoparticles with sizes around 4-7 nm [15]. On the other hand, the Turkevich method [16] is the most used synthesis method of Au nanoparticles, obtaining spherical-shaped morphologies with sizes around 15-20 nm. In this synthesis recipe, Na_3Cit is employed both as a reducing agent and as a stabilizer. These approaches are easily implemented in glasswares but suffered from irreproducibility from batch to batch given their sensitiveness to several factors such as mixing, concentration and temperature gradients, therefore requiring perfect control of the operating conditions [17].

Nowadays, the materials science community has been considering the use of flow chemistry - including microfluidic - as alternative to improve this kind of synthesis [18] due to the advantages offer by the small reaction volumes, the fast reaction rates, the rapid heat and mass transfer, the low operational costs [19], [20], and the possible parallelization and automation opportunities [21]. The microreactor can be fabricated with "on chip" configuration considering various materials depending on the reaction to be performed: polymers

Manuscript received February 28, 2021; revised July 6, 2021; accepted July 25, 2021. Date of publication July 30, 2021; date of current version December 31, 2021. This work was supported in part by the Consejo Nacional de Ciencia y Tecnologia of Mexico (CONACYT) under the Ph.D. Research Scholarship of Gustavo Ochoa-Vazquez (713466) and Project CB-2017-2018-A1-S-39049 and in part by the European Research Council (ERC) through the European Union's Horizon 2020 Research and Innovation Program under Grant 725100 (project Big Mac). *(Corresponding authors: Samuel Marre; Israel López.)*

Gustavo Ochoa-Vazquez is with Universidad Autónoma de Nuevo León, UANL, Centro de Investigación en Biotecnología y Nanotecnología (CIBYN), Laboratorio de Nanociencias y Nanotecnología, Parque de Investigación e Innovación Tecnológica (PIIT), 66629 Apodaca, Nuevo León, Mexico, and also with CNRS, Université Bordeaux, Bordeaux INP, ICMCB, UMR 5026, 33600 Pessac, France.

Boris Kharisov is with the Universidad Autónoma de Nuevo León (UANL), Facultad de Ciencias Químicas, Laboratorio de Materiales I, 66455 San Nicolás de Los Garza, Nuevo León, Mexico.

Ana Arizmendi-Morquecho is with the Centro de Investigación en Materiales Avanzados, S. C. (CIMAV), Unidad Monterrey, Apodaca 66600, Mexico.

Anaïs Cario, Cyril Aymonier, and Samuel Marre are with CNRS, Université Bordeaux, Bordeaux INP, ICMCB, UMR 5026, 33600 Pessac, France (e-mail: samuel.marre@icmcb.cnrs.fr).

Israel López is with the Universidad Autónoma de Nuevo León, UANL, Centro de Investigación en Biotecnología y Nanotecnología (CIBYN), Laboratorio de Nanociencias y Nanotecnología, Parque de Investigación e Innovación Tecnológica (PIIT), 66629 Apodaca, Nuevo León, Mexico (e-mail: israel.lopezhr@uanl.edu.mx).

Digital Object Identifier 10.1109/TNB.2021.3101189

FACULTAD DE CIENCIAS QUÍMICAS

Otorga la presente:

Constancia

A:

Gustavo Ochoa, Israel López

por su participación como ponente con el trabajo:

SÍNTESIS MICROFLUÍDICA: DEL LABORATORIO A LA PALMA DE TU MANO

1er Congreso Internacional de NanoBioIngeniería

Dr. Eduardo Soto Regalado

icmcb

Chimie du solide
Science des matériaux
Sciences moléculaires

Dr Samuel MARRE
Chargé de Recherche CNRS
Supercritical Fluid Group
CNRS - Université de Bordeaux - ICMCB
87 avenue du docteur A. Schweitzer
33607, Pessac, France
Tél. :+33(0)5 40 00 62 94
E-mail : samuel.marre@icmcb.cnrs.fr

Pessac,
le 04 Juillet 2019,

A qui de droit,

Je soussigné, Samuel MARRE, co-organisateur du workshop FLOWMAT 2019 qui s'est tenu à Paris les 26 et 27 Juin 2019, confirme par la présente que Mr Gustavo OCHOA a bien assisté au workshop et a réalisé une présentation de ses travaux de recherche.

Samuel MARRE

FLOWMAT 2019